Caveolin-1 Autonomously Regulates Hippocampal Neurogenesis Via Mitochondrial Dynamics

Terilyn K. L. Stephen[1], Luis Aponte Cofresi[1], Elvis Quiroz[1], Kofi Owusu-Ansah[1], Yomna Ibrahim[1], Ellis Qualls[1], Jeffery Marshall[1], Wenping Li[2], Aashutosh Shetti[1], Jacqueline A Bonds [3], Richard D. Minshall[4,5], Stephanie M. Cologna[2], Orly Lazarov[1,6,*]

[1]Department of Anatomy and Cell Biology, University of Illinois at Chicago, Chicago, IL, USA

[2]Department of Chemistry, University of Illinois at Chicago, IL, USA

[3]Departmet of Anesthesiology, University of California San Diego, CA, USA

[4]Deparment of Pharmacology and Regenerative Medicine, University of Illinois at Chicago, IL,USA

[5]Department of Anesthesiology, University of Illinois at Chicago, IL USA

[6]Lead Contact

[*]Correspondence: olazarov@uic.edu

Keywords

Caveolin-1, Adult Hippocampal Neurogenesis, Neural Stem Cells, Neuronal Differentiation, Mitochondria Dynamics

Summary

The mechanisms underlying adult hippocampal neurogenesis (AHN) are not fully understood. AHN plays instrumental roles in learning and memory. Understanding the signals that regulate AHN has implications for brain function and therapy. Here we show that Caveolin-1 (Cav-1), a protein that is highly enriched in endothelial cells and the principal component of caveolae, autonomously regulates AHN. Conditional deletion of Cav-1 in adult neural progenitor cells (nestin +) led to increased neurogenesis and enhanced performance of mice in contextual discrimination. Proteomic analysis revealed that Cav-1 plays a role in mitochondrial pathways in neural progenitor cells. Importantly, Cav-1 was localized to the mitochondria in neural progenitor cells and modulated mitochondrial fission-fusion, a critical process in neurogenesis. These results suggest that Cav-1 is a novel regulator of AHN and underscore the impact of AHN on cognition.

Introduction

The dentate gyrus (DG) of the adult hippocampus is a dynamic brain region where newly born granule neurons are generated throughout life via the process of adult hippocampus neurogenesis (AHN). Radial glia-like neural stem cells (NSC) and neural progenitor cells (NPCs, together referred to NSPC) reside in the subgranular zone of the DG and undergo proliferation and differentiation to produce new granule neurons [1]. New neurons integrate into hippocampal circuitry and function in context-dependent spatial learning and memory behavioral tasks [2-5]. Neurogenesis declines with age and aging. In mice, significant reductions in NSPC proliferation and newborn neuron generation were documented as early as 5 to 6 months of age [6-8]. Increasing evidence shows that in both humans and rodent models, adult hippocampal neurogenesis is impaired in several brain diseases and disorders including Alzheimer's Disease (AD) [9-12]. In human studies, it has been shown that a reduction in the levels of neuroblasts in the DG associates with worsen cognitive performance in patients diagnosed with mild cognitive impairments or AD compared to healthy aging controls [11]. Interesting, augmentation of hippocampal neurogenesis through either genetic and pharmacologic modulation, environmental enrichment, or voluntary physical activity has been shown to restore hippocampal memory deficits in AD mouse models [13-15]. Despite numerous studies identifying intrinsic and extrinsic cellular modulators of hippocampal neurogenesis [16-20], the mechanisms underlying maintenance of NSPC and neurogenesis-dependent memory function are still not fully understood.

Caveolin-1 (Cav-1) is a 21-24 kDa scaffolding and signaling protein that belongs to the caveolin gene family[21]. Cav-1 generates and maintains caveolae, distinct flask shape invaginations on the plasma membrane, which govern various cellular functions including endocytosis [22,23]. Cav-1 protein expression is found to be highly abundant in the brain

vasculature [24,25] and is essential for blood brain barrier integrity and neurovascular coupling [26-29]. Previously, we showed that Cav-1 protein expression is depleted in the hippocampus of a Type II diabetes mouse model and that rescue of Cav-1 protein expression improved hippocampal memory performance [30]. Global Cav-1 knockout (gCav-1 KO) mice exhibit a wide range of neurological deficits including impairments in cholinergic function and hippocampal plasticity compared to wildtype (WT) controls [31-33]. Moreover, Cav-1 overexpression in hippocampal primary neurons and brain tissue show that Cav-1 promotes dendritic growth and arborization through the enhancement of lipid raft formation and localization of synaptic receptors to lipid rafts on the plasma membrane [34,35]. Few studies exist examining Cav-1 in neurogenic cell types. It has been reported that in the developing cortex, Cav-1 expression is essential for internalization of cell adhesion proteins that regulate proper migration and dendritic pruning in immature neurons [36]. Additionally in early stages of neuronal differentiation from NPCs derived from human iPSCs, Cav-1 phosphorylation at its tyrosine 14 site is needed for axonal growth [37]. However, a role for Cav-1 in AHN has never been described.

Here, we show that Cav-1 is expressed in hippocampal NSPC. Cell - specific deletion of Cav-1 in AHN in mice, resulted in significant reductions in NSC proliferation, increased neuronal differentiation and enhanced performance of mice in the AHN - dependent contextual discrimination behavior task. Proteomic analysis revealed that Cav-1 regulates AHN via mitochondria-related protein pathways. Importantly, we observed that Cav-1 localizes to the mitochondria in NSPCs and regulates their fission-fusion dynamics, critical for neuronal differentiation. This study determines that Cav-1 is a novel regulator of AHN and a new therapeutic target for age-related cognitive decline disorders.

Results

Cav-1 expression in adult hippocampal neural stem cells

We first examined the expression of Cav-1 in hippocampal NSPC by isolating them from adult wild type (WT) mice. We confirmed Cav-1 protein expression by immunostaining (**Figure 1A**). Interestingly, we found that Cav-1 has heterogenous expression in Nestin+ NSPC cells with Cav-1 immunoreactivity characterized by fluorescent puncta distributed throughout the cytoplasm. We show a significant correlation between expression levels of Cav-1 and Nestin where NSPC with elevated Cav-1 expression associate with cells displaying higher levels of Nestin expression and area of Nestin per cell **(Figure 1B-C).** Nestin expression is typically high in actively proliferating NSPC and downregulated as cells exit the cell cycle during differentiation [38,39]. To further investigate the role of Cav-1 in AHN, we generated a NSPC - specific inducible Cav-1 knockout model, where we bred a Cav-1 floxed mice (Cav-1$^{fl/fl}$) [40,41] with a tamoxifen inducible Cre recombinase driven by a Nestin promoter (NestinCre$^{ERT2/+}$) [2,13] (**Figure 1D)**. NestinCre$^{ERT2/+}$;Cav-1$^{fl/fl}$ mice were injected at 4-5 weeks of age with either tamoxifen (TAM) to conditionally delete Cav-1 from NSPCs (iNSC Cav-1 KO) or with corn oil (Corn) to generate control mice (iNSC Cav-1 WT). We confirmed Cav-1 recombination in hippocampal NSPC isolated from iNSC Cav-1 KO and iNSC Cav-1 WT mice by quantitative real-time PCR (qPCR) and immunoblotting **(Figure 1E-G).** We found that isolated hippocampal NSPC from iNSC Cav-1 WT mice had similar Cav-1 expression pattern as WT NSPC with Cav-1 displaying fluorescent puncta **(Figure 1H)**. Ultrastructural transmission electron microscopy was used to determine if Cav-1 expression in NSPC correlated with the presence of caveolae. Flask-shaped invaginations and vesicles resembling caveolae were identified in the iNSC Cav-1 WT NSPC, whereas larger (>150 nm) electron dense vesicles resembling clathrin-coated vesicles were predominantly found in the iNSC Cav-1 KO NSPC **(Figure 1I).** Together, this indicates that Cav-1 is expressed in adult hippocampal NSPCs and correlated with the presence of caveolae, and that tamoxifen-induced recombination leads to a complete deletion of Cav-1 in iNSC Cav-1 KO mice.

Deletion of Cav-1 in NSC leads to reduced NSC proliferation in adult hippocampal neurogenesis

Next, we asked whether the deletion of Cav-1 in NSCs would affect their proliferation. NSCs were identified by the co-expression of glial fibrillary acidic protein (GFAP) and Nestin in the subgranular layer (SGL) of the DG. In contrast to quiescent, proliferating NSCs also expressed the mitosis-linked minichromosome maintenance complex component 2 (MCM2). Quantitative stereology at 3 months **(Figure 2A**, 60 dpi of Tam**)** of age revealed no significant difference in the total NSC population ($GFAP^{+}Nestin^{+}$) and the quiescent NSC sub-population ($GFAP^{+}Nestin^{+}MCM2^{-}$) between iNSC Cav-1 KO vs iNSC Cav-1 WT mice **(Figure 2B-D)**. However, a significant reduction in the number of proliferating NSC ($GFAP^{+}Nestin^{+}MCM2^{+}$) was observed in the iNSC Cav-1 KO mice **(Figure 2E)**. Similarly at 6 months of age, no differences in the total NSC population ($GFAP^{+}Nestin^{+}$) and quiescent sub-population ($GFAP^{+}Nestin^{+}MCM2^{-}$) was observed, yet the number of proliferating NSC ($GFAP^{+}Nestin^{+}MCM2^{+}$) was significantly reduced in the iNSC Cav-1 KO mice compared to iNSC Cav-1 WT controls (**Figure 2F-I)**. In support of these results, neurosphere cultures isolated from the iNSC Cav-1 KO mice showed reduction in clone formation, clone diameter and cell number compared to iNSC Cav-1 WT mice (**Figure 2J-M**). In addition, we examined the level of proliferation of neurosphere cultures derived from iNSC Cav-1 WT and iNSC Cav-1 KO NSPC using 1 hr pulse with EdU (5-ethynyl-2'-deoxyuridine). We found that the number of EdU+ cells was significantly lower in iNSC Cav-1 KO NSPC compared to iNSC Cav-1 WT NSPC **(Figure 2N-O).** Interestingly, we observed that EdU fluorescence intensity, previously shown to correlate with length of S-phase [42], was significantly higher in EdU+ cells in iNSC Cav-1 KO **(Figure 2P),** suggesting that Cav-1 may regulate cell cycle kinetics. Taken together, these findings show that Cav-1 deletion affects the extent of proliferation of hippocampal NSC in the DG.

iNSC Cav-1 KO mice display increased differentiation of hippocampal NSPC

Given that reduced proliferation of NSPC can influence levels of neurogenesis, we sought to determine whether Cav-1 deletion in NSPC leads to alterations in the formation of new granule neurons in the adult DG. At 3-months of age, the iNSC Cav-1 KO and iNSC Cav-1 WT mice showed no significant changes in the number of neuroblasts or immature neurons in the DG (**Figure S1).** However, at 6 months of age the iNSC Cav-1 KO mice exhibited a significant increase in total number of DCX^+ NPCs, neuroblasts (DCX+NeuN-) and immature neurons (DCX+NeuN+) compared to iNSC Cav-1 WT mice (**Figure 3A-D**). The effect of Cav-1 deletion on differentiation was also examined in hippocampal neurosphere cultures isolated from iNSC Cav-1 WT and iNSC Cav-1 KO mice as similarly described[43,44] (**Figure 3E**). Interestingly, *Cav-1* transcript and protein expression were significantly decreased as iNSC Cav-1 WT NSPC underwent differentiation for 5-7 days **(Figure 3F, I, J).** The progression of differentiation was validated by reduced expression of nestin and Sox2 (**Figure 3G,I,K)** and increased expression of Map2 and β-III-tubulin (**Figure 3H,I,L**)**.** In support of the observations in brain sections, the expression of Map2 and β-III-tubulin was significantly higher in differentiating NSPC iNSC Cav-1 KO, compared to WT (**Figure 3H,I,L**) **.**

We next investigated whether Cav-1 deletion in NSPCs altered the early stages of differentiation leading to the increase in immature granule neurons we observed in iNSC Cav-1 KO mice. We utilized a 5-bromo-2'-deoxyuridine (BrdU) pulse labeling paradigm where mice received a daily BrdU injection for 12-days and sacrificed 24 hr after the last injection (**Figure 4A**). A trending reduction ($p = 0.05$) in the total level of BrdU positive cells in the DG was observed in the iNSC Cav-1 KO mice compared to the iNSC Cav-1 WT mice (**Figure 4B,C**). Consistent with our proliferation analysis, $BrdU^+$ NSCs ($GFAP^+Sox2^+$) were significantly decreased in the iNSC Cav-1 KO mice compared to iNSC Cav-1 WT (**Figure 4D,E**). A trending decrease ($p=0.07$) in the total number of $BrdU^+$ NPCs ($GFAP^-Sox2^+$) was also observed in the

iNSC Cav-1 KO compared to iNSC Cav-1 WT mice (**Figure 4F**). Notably, a significant increase in the ratio of BrdU retaining non-NSPCs (BrdU+GFAP$^-$Sox2$^-$) to total levels of BrdU was observed in the iNSC Cav-1 KO mice (**Figure 4G**). To examine if this enhanced proliferation is of neuroblasts, we examined co-expression of BrdU, DCX and NeuN (Figure 3H). There was no change in the number of BrdU+DCX$^+$NeuN- NPC/neuroblasts (**Figure 4I**). Yet, the number of BrdU$^+$DCX$^+$NeuN$^+$ immature neurons was significantly increased in the iNSC Cav-1 KO mice compared to iNSC Cav-1 WT (**Figure 4J-K**). Taken together, this data confirms that Cav-1 is a negative regulator of neuron differentiation and Cav-1 loss drives adult hippocampal neurogenesis.

Conditional deletion of Cav-1 in NSC improves context discrimination learning and memory

Hippocampal neurogenesis is essential for the discrimination of similar contexts (pattern separation), where newborn granule neurons (4-6 weeks post-mitotic) become selectively activated during memory formation[2,45,46]. To test whether the increase in immature neurons in the iNSC Cav-1 KO mice results in improved learning and memory, iNSC Cav-1 KO and iNSC Cav-1 WT mice underwent a modified fear conditioning test[47] **(Figure 5A).** Both iNSC Cav-1 KO and iNSC Cav-1 WT mice displayed higher freezing levels in Context A (Cxt A) compared to Context B (Cxt B) at 30 mins post-shock **(Figure 5B).** No difference in the discrimination index between each group was observed at 30 mins post-shock on Day 2 **(Figure 5C)**. Interestingly, the iNSC Cav-1 KO mice had a significantly higher level of freezing in Cxt A compared to Cxt B at 24 hr post-shock whereas the iNSC Cav-1 WT mice exhibited the equal amount of freezing in both Cxt A and Cxt B **(Figure 5D)**. Analysis of the discrimination index revealed a trending increase in the iNSC Cav-1 KO mice compared to iNSC Cav-1 WT mice **(Figure 5E),** suggesting that enhanced generation of newborn neurons in the iNSC Cav-1 KO mice improved neurogenesis-dependent learning and memory.

We then examined whether the iNSC Cav-1 KO mice displayed enhanced context generalization compared to the iNSC Cav-1 WT mice 24 hr post-shock. Studies show that significant alterations in context geometry are sufficient to induce generalization behavior[48,49] and that newborn granule neurons in the hippocampus are found to maintain generalization behavior[50]. iNSC Cav-1 KO and iNSC Cav-1 WT mice underwent the same context discrimination paradigm at 6 months of age except Cxt B was exchanged for Context C (Cxt C) in which the geometry had been changed from a square to a circle and the floor covered with a plastic sheet **(Figure 5F).** Interestingly on Day 2, iNSC Cav-1 WT mice were unable to discriminate Cxt A from Cxt C 30 min post-shock whereas iNSC Cav-1 KO mice had a significantly higher level of freezing in Cxt A compared to Cxt C with a trending significant discrimination index **(Figure 5G-H)**. On Day 3, both groups of mice were able to equally discriminate Cxt A from Cxt C 24 hr post-shock with no difference in the discrimination ratio **(Figure 5I-J).** No differences in level of anxiety-like behavior **(Figure S2A-D)** nor performance in the spatial novel object location (NOL) task (**Figure S2E-G**) were observed between the iNSC Cav-1 KO and iNSC Cav-1 WT mice. These findings suggest that Cav-1 deletion in NSPCs results in an increase in the number of immature neurons, which in turn, leads to improved neurogenesis-dependent context discrimination.

Proteomic analysis indicates that Cav-1 regulates mitochondrial and cellular metabolism pathways in hippocampal NSPCs

Building on our findings that Cav-1 deletion in NSPCs enhances hippocampal neurogenesis, we hypothesized that Cav-1 regulates pathways involved cell cycle and differentiation in NSPCs. We used quantitative proteomics to assess the molecular mechanisms by which Cav-1 regulates neurogenesis **(Figure 6A).** A total of 4730 proteins were identified in the iNSC Cav-1 KO and iNSC Cav-1 WT NSPC with 326 proteins identified as differentially expressed (DEP) **(Figure 6B, Table S1, ANOVA, $p < 0.05$**). Of the 326 DEPs, 228 proteins

were downregulated, and 98 proteins were upregulated in the iNSC Cav-1 KO NSPCs compared to WT NSPCs. Next, we performed functional enrichment analysis of DEPs using Ingenuity Pathway Analysis (IPA) and Gene Ontology (GO) pathway and cluster mapping. Interestingly, the top 4 significantly altered IPA pathways included Mitochondrial Dysfunction, TCA Cycle II (Eukaryotic), Superpathway of Cholesterol Biosynthesis, and Oxidative Phosphorylation **(Figure 6C, Table S2).** GO analysis revealed significantly altered pathways related to the ATP biosynthesis, electron transport chain (ETC), mitochondria and ribosome subunits and lipid oxidation **(Figure 6D, Table S3)**.

To further investigate the role of Cav-1 in regulating mitochondria proteins, we compared the DEPs to the MitoCarta3.0 gene dataset[51]. Mitocarta3.0 is a curated inventory based on genomic data, mass spectrometry, and microcopy data of 1140 mouse genes localized to mitochondria. We identified 84 of the 326 DEPs (24% of total DEP) in the MitoCarta 3.0 gene dataset **(Figure 6E).** We found that proteins involved in mitochondrial DNA (mtDNA) maintenance, mitochondrial RNA (mtRNA) and translation pathways were downregulated in the iNSC Cav-1 KO NSPCs compared to Cav-1 WT (**Figure 6F,G, Table S4**). Similarly, proteins involved in mitochondria protein import, sorting and homeostasis, and signaling and molecule transport were downregulated in the iNSC Cav-1 KO compared to iNSC Cav-1 WT NSPC **(Figure 6E,F, Table S4).** Several DEPs categorized in metabolism pathways including glycolysis, TCA, OXPHOS, carbohydrate, lipid, nucleotide, amino acid, vitamin, and metal metabolism pathways were also downregulated in the iNSC Cav-1 KO NSPCs compared to iNSC Cav-1 WT NSPCs **(Figure 6F,G, Table S4)**. Noticeably, we found that mitochondrial dynamics and surveillance associated proteins including Metaxin-2 (MTX2) and Voltage-dependent Anion-selective Channel (Vdac1) were downregulated, whereas Mitochondrial Rho GTPase 2 (Rhot2, also called Miro2) was significantly enriched in the iNSC Cav-1 KO NSPCs compared to iNSC Cav-1 WT NSPCs (**Figure 6E,G, Table S4)**. Miro2 interacts with mitofusion-2 (Mfn-2) to coordinate fission/fusion events[52] and in neurons, Miro2 is required for retrograde

trafficking of mitochondria[53,54]. Taken together, our proteomic findings show that Cav-1 may play a role in pathways involved in mitochondria homeostasis, metabolism, and dynamics in hippocampal NSPC.

Next, to validate the proteomics data and establish the specific signals regulated by Cav-1, we examined the expression of glycolytic and TCA cycle proteins including lactate dehydrogenate (LDHA), hexokinase 2 (HK2), pyruvate dehydrogenase (PDH), and aconitase 2 (ACO2) in hippocampal NSPC isolated from iNSC Cav-1 KO and iNSC Cav-1 WT mice using Western blot analysis. Expression levels of LDHA, HK2, PDH were comparable in NSPCs isolated from iNSC Cav-1 KO compared to iNSC Cav-1 WT mice **(Figure S3A-F)**. However, expression of ACO2 was significantly decreased in hippocampal NSPC lacking Cav-1 expression. Next, we examined oxidative phosphorylation in NSPC extracts using a total OXPHOS antibody cocktail that detects proteins in Complex I (CI-NDUF8a), Complex II (CII-SDHB), Complex III (CIII-UQCR2), Complex IV (CIV-MTCO) and Complex V (CV-ATP5a) **(Figure S3G).** iNSC Cav-1 KO NSPCs showed significant reductions in CIII-UQCR2 and CIV-MTCO1 compared to iNSC Cav-1 WT NSPCs (**Figure S3H)**. No significant changes in CII-SDHB were found, however, a trending upregulation ($p = 0.05$) of CV-ATP5a expression was detected in iNSC Cav-1 KO NSPCs compared to iNSC Cav-1 WT NSPCs (**Figure S3I-K**). Interestingly, expression of CI-NDUF8a was not detected in NSPCs isolated from either iNSC Cav-1 KO or iNSC Cav-1 WT mice. Furthermore, using the Agilent Seahorse Real-Time ATP Rate Assay we measured changes in glycolysis and mitochondrial (oxidative phosphorylation) ATP production (**Figure S3L-M**). Extracellular acidification (ECAR) and basal oxygen consumption rate (OCR) **(Figure S3L-O),** as well as glycolysis and mitochondrial ATP production **(Figure S3M)** were comparable in iNSC Cav-1 KO and iNSC Cav-1 WT NSPCs. Next, we examined the expression of mitochondrial dynamics and surveillance including Drp-1, the primary regulator of fission, and mfn-2, a main regulator of fusion in the iNSC Cav-1 KO and

iNSC Cav-1 WT NSPCs via immunoblotting (**Figure S4A-D**). We observed a significant increase the in Drp-1 expression, yet no alterations in Mfn-2 expression in the iNSC Cav-1 KO NSPCs compared to WT (**Figure S4C,D**). Expression levels of Miro2 and VDAC1 were also assessed as these proteins function in mitochondria calcium signaling and trafficking, which are necessary for mitochondria homeostasis and balanced fission and fusion[55]. A trending increase was observed in Miro2 expression in the iNSC Cav-1 KO cells where no differences in VDAC expression was found (**Figure S4E,F**). Together this data suggests that Cav-1 is a critical regulator of proteins involved in mitochondrial fission/fusion dynamics in hippocampal NSPCs.

Cav-1 regulates mitochondrial morphology in hippocampal NSPC

In hippocampal neurogenesis, changes in mitochondrial morphology and dynamics have been found to govern self-renewal and cell fate[56]. To begin investigating the role of Cav-1 in mitochondrial morphology and dynamics in NSPCs, we first examined the co-localization of Cav-1 to mitochondria. Caveolae and caveolin-1 were previously shown to localize to the outer membrane of mitochondria[57,58]. We show that Cav-1 co-localizes with Mitochondrial import receptor subunit TOM20 homolog (Tom-20), a translocase located on the mitochondrial outer membrane mitochondria, in WT hippocampal NSPCs by utilizing 3D confocal microcopy (**Figure 7A**). The average Mander's Correlation Coefficient between Cav-1 and Tom-20 was 0.2513 implying that ~25% of the Cav-1 fluorescence signal overlaps with Tom-20 **(Figure 7A).** In light of this result, we examined Cav-1 protein expression in isolated mitochondrial membranes from WT hippocampal NSPCs **(Figure 7B).** The majority of Cav-1 expression was observed in the mitochondrial fraction **(Figure 7B).** Interestingly, the majority of Drp-1 was found in the cytosolic rather than the mitochondrial fraction **(Figure 7B).** The mitochondrial and cytosol enriched fractions were confirmed by Tom-20 and Drp-1. Drp-1 and Mfn-2 are recruited to the outer membrane of the mitochondria to induce morphological changes and movement by alteration of fission-fusion events through contact sites between mitochondria, the endoplasmic reticulum,

and the cytoplasm[59]. Taken together with the observation that total levels of Drp-1 were increased in protein lysates of iNSC Cav-1KO compared to WT (**Figure S4**), we asked whether Drp-1 and Mfn-2 have altered recruitment to the mitochondria in hippocampal NSPCs lacking Cav-1 expression. Mitochondria and cytosol enriched fractions were isolated from iNSC Cav-1 KO and iNSC Cav-1 WT NSPCs (**Figure 7C)**. iNSC Cav-1 KO NSPCs had elevated Drp-1 expression in the cytosol fraction and reduced Drp-1 expression in the mitochondrial faction compared to WT (**Figure 7D,E)**. In contrast, iNSC Cav-1 KO cells had reduced Mfn-2 expression in the cytosol fraction and elevated expression in the mitochondria faction compared to WT **(Figure 7B-E**). In light of these results, we examined whether Cav-1 deletion in hippocampal NSPCs alters mitochondrial morphology by ultrastructural electron microscopy. We show that the number of mitochondria per cell imaged was significantly reduced in the iNSC Cav-1 KO NSPC compared to iNSC Cav-1 WT NSPC yet, the mitochondrial area and perimeter was significantly increased in the iNSC Cav-1 KO NSPCs (**Figure 7F, S5A-C**). A reduction in a circularity was also observed in the iNSC Cav-1 KO NSPCs (**Figure S5D),** which is indicative of elliptical shape compared to the iNSC Cav-1 WT NSPC. To further build on our findings, live cell imaging with the fluorescent dye tetramethyl rhodamine methylester (TMRM) was utilized to observe mitochondrial morphology, membrane potential and velocity in live NSPCs **(Figure 7G**). Similar to our ultrastructural findings, mitochondria in iNSC Cav-1 KO NSPC exhibited a significant increase in area **(Figure 7H)**, perimeter per cell **(Figure 7I)** and elliptical shape **(Figure 7J)** compared to the iNSC Cav-1 WT NSPCs**.** Further, mitochondria in the iNSC Cav-1 KO NSPC had an increase in branch length compared to WT NSPCs (**Figure 7K).** iNSC Cav-1 KO NSPCs exhibited higher levels of TMRM fluorescence intensity suggesting a higher, hyperpolarized, mitochondrial membrane potential compared to WT NSPCs (**Figure 7L**). Time-lapse imaging of mitochondria was analyzed using the Trackmate plugin in ImageJ[60] (**Figure 7M, Video S1, Video S2)**. Mitochondria in the iNSC Cav-1 KO NSPC had a significant increase in velocity and total distance traveled compared to iNSC Cav-1 WT NSPCs **(Figure 7N,O**).

Taken together with previous reports that mitochondrial fusion takes place during neuronal differentiation [61], our results suggest that the deletion of Cav-1 in NSPCs facilitates neuronal differentiation by inducing mitochondrial fusion.

Discussion

This study revealed several significant observations. First, we observed that Cav-1 is expressed in hippocampal NSPCs. Levels of Cav-1 correlated with nestin expression and were downregulated upon neuronal differentiation. Second, we showed evidence that Cav-1 has a cell-autonomous role in regulating NSPC differentiation in the adult DG. Cav-1 deletion in NSPCs resulted in reduced number of proliferating NSPCs and enhanced number of neuroblasts and immature neurons in the DG, which is suggestive that Cav-1 expression in NSPCs negatively regulates differentiation. This finding was further supported by increased expression of Map2 and β-III-tubulin in differentiating iNSC Cav-1 KO NSPCs compared to WT. The increase in number of immature neurons was manifested as improved context discrimination performance. Third, we showed that Cav-1 regulates mitochondrial protein networks in NSPCs. Additionally, we observed that deletion of Cav-1 in NSPCs resulted in elongated mitochondria, suggesting enhanced fusion, as well as increased mitochondria velocity and distance traveled. In support of enhanced fusion, we observe that deletion of Cav-1 led to increased Mfn-2 in mitochondria isolated from NSPCs. Our results suggest that Cav-1 plays a role in the recruitment of Drp-1 and Mfn-2 to the mitochondria, providing evidence that Cav-1 may be a key determinate of mitochondrial dynamics in hippocampal NSPCs.

The balance of quiescence, proliferation, and differentiation of NSCs is essential for the maintenance of hippocampal neurogenesis. NSCs integrate a variety of extrinsic and intrinsic signals to determine cell fate and lineage[62]. Cav-1 is enriched in endothelial cells, and thus, may

have a non-cell autonomous role in regulation of hippocampal neurogenesis. Our studies show that Cav-1 acts as an intrinsic signal regulating the differentiation of NSPCs in the DG. The transition of NSC from quiescence to proliferation (activation) or vice versa, is closely linked to the G_0-G_1-S checkpoints of the cell cycle[63]. In fibroblasts, studies show that expression of Cav-1 induces arrest at the G_0-G_1 phase and inhibits proliferation through p53/p21-dependent signaling[64]. In contrast, cancer studies reveal that Cav-1 depletion causes G_0-G_1 cell cycle arrest and impaired proliferation[65]. Cav-1 function in hematopoietic stem cells also regulates cell cycle progression at the G_2-M phase and deletion impairs quiescence and differentiation[66]. Our observations showed that the deletion of Cav-1 resulted in reduced number of BrdU+ NSPCs, while it increased the number of BrdU+ immature neurons. This could be the result of a few mechanisms, including an elongated S phase or reduced division events per cell. Our *in vitro* studies showing a reduction in the number of EdU positive cells, but a higher signal intensity in iNSC Cav-1KO support these options. In addition, the increase in BrdU+ committed cells may suggest a faster exit from the cell cycle. Our studies show that the quiescent NSC pool is preserved in the iNSC Cav-1 KO mouse at 6 months of age. While Cav-1 deletion causes a decrease in the number of proliferating NSCs, the total number of NSCs is comparable between the iNSC Cav-1 KO or WT. This phenotype has also been documented in studies ablating BMPRII receptors in NSC where the rate of immature neuron generation is increased but no alterations in the NSC pool were observed[67]. That said, we cannot exclude the possibility that with time the NSC pool becomes exhausted. Additional studies are warranted to examine the effect of Cav-1 deletion in NSC on cell cycle progression as well as the transition between quiescent to proliferative NSCs.

Augmentation of neurogenesis improves context discrimination[2]. Thus, we examined whether the increase in number of immature neurons in iNSC Cav-1 KO mice improved learning and memory. We observed that the iNSC Cav-1 KO mice exhibit enhanced discrimination when contexts are similar but preformed equally to WT mice in spatial recognition memory and

context generalization. These results support the notion that increased neurogenesis improves neurogenesis-dependent contextual discrimination[68].

Recent studies suggest that changes in mitochondrial morphology impact stem cell identity and cell fate, and that mitochondrial fusion drives neuronal differentiation [56,61,69]. NSC in the adult DG exhibit fragmented and globular mitochondria that become more elongated as cells progress into committed NPCs and immature neurons[70]. *In vivo* and *in vitro* studies show that when NSPC differentiate into neurons a metabolic switch occurs from glycolysis to OXPHOS[70,71]. Fragmented morphology is often exhibited when cells utilize glycolysis for ATP generation whereas elongated mitochondria signify OXPHOS dependence and the electron transport chain[69]. We observed that NSPC lacking Cav-1 have elongated mitochondria and increased mitochondria membrane potential compared to controls which is suggestive of a neuronal phenotype. However, our findings did not show a robust downregulation of glycolytic proteins LDHA and HK2 or upregulation of OXPHOS proteins. This result could be the result of the asynchronous nature of cultures grown in proliferative media lacking factors for bulk neuronal induction. Future experiments should address mitochondria morphology, glycolysis rate and ATP rate in both NSPC lacking Cav-1 and WT under differentiation conditions. Additionally, less is known about the metabolic profile and mitochondrial dynamics of quiescent or non-dividing NSPCs. Protocols inducing quiescence in primary hippocampal NSPCs have been developed[72] warranting the evaluation of Cav-1 in the regulation of metabolism and morphology in various stages of cell fate. Intriguingly, elongation of mitochondria observed in iNSC Cav-1KO NSPCs coincided with upregulated translocation of Mfn-2 to the mitochondria, while the majority of Drp-1 that facilitates fission was found in the cytosol. Taken together, this suggests that loss of Cav-1 in NSPCs facilitates mitochondrial fusion. Our results are in agreement with another study that shows that downregulation of Cav-1 inhibits Drp-1 function by increasing phosphorylation at Ser637 and thus, promoting mitochondrial fusion[73]. We observed that Drp-1 was significantly upregulated in the cytosol of iNSC Cav-1 KO NSPC yet no

changes in Drp-1 mitochondrial localization were observed compared to control NSPCs. Upregulation of Drp-1 expression has been observed during neuronal differentiation[74] but it is undetermined if this is a result of Cav-1 downregulation or if this alteration impairs Drp-1 function to regulate mitochondrial morphology. A recent study shows that Cav-1 is a negative regulator of mitochondria endoplasmic reticulum remodeling leading to interference of Drp1 phosphorylation and cellular distribution[75]. It is unknown whether Cav-1 deletion in hippocampal NSPCs alters phosphorylation dependent activation or inhibition of Drp-1 or interactions with other fission/fusion related proteins such as mitochondrial fission factor (Mff) or mitochondrial fission protein 1 (Fis1). Future studies should examine these proteins in iNSC Cav-1 KO and iNSC Cav-1 WT NSPCs as well as determine whether rescue of Cav-1 restores Drp-1 signaling and balance of mitochondria dynamics.

In conclusion, this study shows that Cav-1 is a novel autonomous regulator of adult hippocampal neurogenesis that resides in the outer membrane of mitochondria where it regulates morphology and dynamics.

Acknowledgments

We thank Dr. Trongha Phan for his expertise and guidance on behavioral experiments and scientific discussion. We thank Dr. Pavan Kumar, Dr. Muskan Gupta, Abhi Ramakrishnan, Stephanie Dunning for help with animal husbandry, genotyping, and IP injections. We thank Karen Rakowiecki for assistance with cell culture experiments. We thank Dr. Christian Peters and Shana Netherton for use of Elevated Plus Maze equipment. We thank Dr. Ying Jiang for expertise and guidance on the mitochondrial assays. We also thank Dr. Peter Toth and Dr. Ke Ma at the UIC Fluorescence Imaging Core for guidance on microscopy imaging, Figen Seiler at the UIC Electron Microscopy Core for TEM imaging, and Dr. Balaji Ganesh at the UIC Flow Cytometry Core for assistance with the Mitochondria Seahorse Assay. Graphical abstract, Figure 2A, 3A, and 4E were created Biorender.com. This work was financially supported by

National Institutes of Health, National Institution on Aging (NIA) F30AG071144 (TKLS), T32AG067468, AG033570, AG076940, AG062251, AG060238 (OL), NINDS/NIA:R01NS114413 (SMC) and Together Strong NPC Foundation (SMC).

Author Contributions

TKLS performed the experiments, analyzed the data and wrote the manuscript. LA, EQ, YI, KO, EQ, JM and WL assisted with data collection and analysis. AS and JB assisted with the design of the studies and generation of the mouse models used. RDM and SMC assisted with the data analysis, interpretation, and revision of the manuscript. OL supervised the project, assisted with the data analysis, interpretation and revised the manuscript. All authors contributed to the review of the manuscript.

Declarations of Interests

The authors declare no conflict of interests.

Figure Titles and Legends

Figure 1. Characterization of Cav-1 expression in adult hippocampal NSPC.

(A) Expression of Cav-1 in WT hippocampal NSPC shown by confocal imaging of Cav-1 (green), Nestin (red), and DAPI (blue). Scale bar, 20 μm.

(B-C) Correlation plot of Cav-1 fluorescence intensity per cell by nestin signal intensity per cell (B) and nestin area per cell (C). Each dot represents the fluorescence intensity of an individual cell analyzed from WT mice (n=26 cells).

(D) Schematic of NestinCre$^{ERT2/+}$;Cav-1$^{fl/fl}$ mice, where mice were injected at 4-5 weeks of age with either corn oil (Corn) or tamoxifen (TAM) for 5 consecutive days to generate control mice (iNSC Cav-1 WT) and Cav-1 knockout mice (iNSC Cav-1 KO), respectively.

(E) RT-qPCR quantification of Cav-1 transcript expression from NSPC isolated from the iNSC Cav-1 KO and iNSC Cav-1 WT mice.

(F-G) Cav-1 immunoblot and quantification normalized to β-actin of protein lysate from NSPC isolated from the iNSC Cav-1 KO and iNSC Cav-1 WT mice.

(H) Immunocytochemistry of Cav-1 and confocal imaging of Cav-1 (green) and DAPI (blue) in hippocampal NSPC isolated from iNSC Cav-1 WT and iNSC Cav-1 KO mice shown. Scale bar, 20 μm.

(I) Ultrastructural electron micrographs of caveolae and clathrin coated vesicles in hippocampal NSPC isolated from iNSC Cav-1 WT and iNSC Cav-1 KO mice. Solid green arrowhead indicate caveolae. Open green arrowhead indicate clathrin coated vesicle. Scale bar, 200 nm.

Data represented as mean ± SEM. Data analyzed by Spearman Correlation Analysis (B-C) **$p < 0.01$ and unpaired two-tailed Student's t-test (D-G). **$p < 0.01$, ****$p < 0.0001$.

Figure 2. iNSC Cav-1 KO mice have reduced levels of proliferating NSC in the dentate gyrus.

(A) Strategy to quantify NSC populations in dentate gyrus (DG) of iNSC Cav-1 WT and iNSC Cav-1 KO mice at 3 and 6 months of age.

(B) Representative confocal images of GFAP (white), Nestin (red), MCM2 (green) and DAPI (blue) markers in the DG of iNSC Cav-1 WT and iNSC Cav-1 KO mice at 3 months of age. Yellow arrowheads indicate $GFAP^+Nestin^+MCM2^+$ cells. Scale bar, 25 μm.

(C-E) Quantification of total NSC ($GFAP^+Nestin^+$), quiescent NSC ($GFAP^+Nestin^+MCM2^-$) and proliferating NSC ($GFAP^+Nestin^+MCM2^+$) in the DG of iNSC Cav-1 WT and iNSC Cav-1 KO mice at 3 months of age. n=5 mice per group.

(F) Representative confocal images of GFAP (white), Nestin (red), MCM2 (green) and DAPI (blue) positive cells in the DG of iNSC Cav-1 WT and iNSC Cav-1 KO mice at 3 months of age. Yellow arrowheads indicate $GFAP^+Nestin^+MCM2^+$ cells. Scale bar, 25 μm.

(G-I) Quantification of total NSC ($GFAP^+Nestin^+$), quiescent NSC ($GFAP^+Nestin^+MCM2^-$) and proliferating NSC ($GFAP^+Nestin^+MCM2^+$) in the DG of iNSC Cav-1 WT and iNSC Cav-1 KO mice at 6 months of age. n=5 mice per group.

(J-M) Clonogenic proliferation assay in NSPC isolated from iNSC Cav-1 WT and iNSC Cav-1 KO mice. The number of clones (neurospheres) (L), average clone diameter (M) and number of cells after dissociation of clones (N) on day 5 of the assay were quantified per well. Scale bar, 100 µm.

(N-P) EdU uptake assay in NSPC isolated from iNSC Cav-1 WT and iNSC Cav-1 KO mice. (O) Quantification of the percentage of EdU+ cells to the total DAPI between NSPC isolated from iNSC Cav-1 WT and iNSC Cav-1 KO mice. (P) EdU fluorescence intensity per DAPI nuclei between NSPC isolated from iNSC Cav-1 WT and iNSC Cav-1 KO mice. Scale bar, 20 µm.

Data represented as mean ± SEM. Data analyzed by unpaired two-tailed Student's t-test. ns $p > 0.05$, *$p < 0.05$, **$p < 0.01$, ***$p < 0.001$ ****$p < 0.0001$.

Figure 3. Cav-1 regulates differentiation of hippocampal NSPCs.

(A) Confocal images of DCX and NeuN immunostaining in the DG of iNSC Cav-1 WT and iNSC Cav-1 KO mice at 6 months of age. Scale bar, 25 µm.

(B-D) Quantification of NPCs and neuroblasts (DCX^+NeuN^-) and immature neurons (DCX+NeuN+) and total DCX expressing cells in the DG of iNSC Cav-1 WT and iNSC Cav-1 KO mice. n=4 mice per group.

(E) Schematic representation of the protocol used for neural differentiation of primary hippocampal NSPCs.

(F-H) Quantification of Cav-1, Nestin, and MAP2 transcript expression by RT-qPCR between iNSC Cav-1 WT and iNSC Cav-1 KO NSPCs undergoing differentiation for 5 days. Expression level normalized to d0 of iNSC Cav-1 WT NSPC (n=3 replicates).

(I) Immunoblot of Cav-1, Sox2 and β-III-Tubulin in NSPC isolated from iNSC Cav-1 KO and iNSC Cav-1 WT mice undergoing differentiation for 7 days.

(J-L) Quantification of Cav-1, Sox2 and β-III-Tubulin normalized to GAPDH expression and then normalized to d0 iNSC Cav-1 WT NSPC (n=3 replicates).

Data represented as mean ± SEM. Data analyzed by unpaired two-tailed Student's t-test (B-D) and two-way ANOVA with Tukey multiple comparisons correction (F-G and J-L). ns $p > 0.05$, *$p < 0.05$, **$p < 0.01$, ***$p < 0.001$, and ****$p < 0.0001$.

Figure 4. Deletion of Cav-1 in NSC causes premature differentiation of newborn neurons in the dentate gyrus.

(A) 5-bromo-2'-deoxyuridine (BrdU) pulse strategy to quantify changes in NSC fate and differentiation in DG of iNSC Cav-1 WT and iNSC Cav-1 KO mice at 6 months of age. Mice were injected daily for 12 consecutive days and sacrificed 24 hr after the last injection.

(B-C) Confocal images of BrdU immunostaining and quantification total number of $BrdU^+$ cells in the DG of 6-month-old iNSC Cav-1 KO and iNSC Cav-1 WT mice. Scale bar, 25 µm. n=4 mice per group.

(D) Representative confocal images of BrdU (red), Sox2 (white), GFAP (green) and DAPI (blue) markers in the DG of iNSC Cav-1 WT and iNSC Cav-1 KO mice at 6 months of age. Solid yellow arrowheads indicate $BrdU^+GFAP^+Sox2^+$ cells. Outlined yellow arrowheads indicate $BrdU^+GFAP^-Sox2^-$ cells. Scale bar, 25 µm.

(E-G) Quantification of total $BrdU^+$ NSCs ($GFAP^+Sox2^+$), $BrdU^+$ NPCs ($GFAP^+Sox2^-$) and percentage of $BrdU^+$ cell phenotypes normalized to total number of $BrdU^+$ cells in the DG of iNSC Cav-1 WT and iNSC Cav-1 KO mice. n=4 mice per group.

(H) Representative confocal images of BrdU (white), DCX (Green), NeuN (red) and DAPI (blue) markers in the DG of iNSC Cav-1 WT and iNSC Cav-1 KO mice at 6 months of age. Outlined yellow arrowheads indicate $BrdU^+DCX^+NeuN^+$ cells. Scale bar, 25 µm.

(I-K) Quantification of $BrdU^+$ DCX expressing NPCs and neuroblasts (DCX^+NeuN^-), immature neurons (DCX+NeuN+), and percentage of $BrdU^+$ immature neurons (DCX+NeuN+) normalized to total number of BrdU + cells in the DG of iNSC Cav-1 WT and iNSC Cav-1 KO mice. n=4 mice per group.

Data represented as mean ± SEM. Data analyzed by unpaired two-tailed Student's t-test, except (G) which was analyzed by two-way ANOVA with Tukey multiple comparisons correction. ns $p > 0.05$, *$p < 0.05$, and **$p < 0.01$.

Figure 5. iNSC Cav-1 KO mice display enhanced contextual discrimination learning and memory.

(A) Schematic of contextual fear discrimination paradigm between Context A and B. See Materials and methods for details.

(B-C) Quantification of percent freeze (30 min post-shock) and discrimination index in context A and B on Day 2 between the NSC Cav-1 WT and iNSC Cav-1 KO mice. n=12 per genotype.

(D-E) Quantification of percent freeze (24 hr post-shock) and discrimination index in context A and B on Day 3 between the NSC Cav-1 WT and iNSC Cav-1 KO mice. n=12 per genotype.

(F) Schematic of contextual fear generalization paradigm between Context A and C. See Materials and methods for details.

(G-H) Quantification of percent freeze (30 min post-shock) and discrimination index in context A and C on Day 2 between the NSC Cav-1 WT and iNSC Cav-1 KO mice. n=12 iNSC Cav-1 WT and n=8 iNSC Cav-1 KO.

(H-I) Quantification of percent freeze (24 hr post-shock) and discrimination index in context A and C on Day 3 between the NSC Cav-1 WT and iNSC Cav-1 KO mice. n=12 iNSC Cav-1 WT and n=8 iNSC Cav-1 KO.

Data represented as mean ± SEM. Data analyzed in by two-way ANOVA with Tukey's multiple comparisons correction expect for data in C,E,H,J which was analyzed by unpaired two-tailed Student's t-test. ns $p > 0.05$, *$p < 0.05$, **$p < 0.01$ and ***$p < 0.001$.

Figure 6. Expression of mitochondria and metabolism related proteins are altered in hippocampal NSPCs lacking Cav-1.

(A) Schematic of proteomic workflow for hippocampal NSPCs isolated from iNSC Cav-1 KO and iNSC Cav-1 WT mice. See Materials and methods for details.

(B) Volcano plot of proteins identified in iNSC Cav-1 KO vs iNSC Cav-1 WT cells. Significantly upregulated proteins in red and significantly downregulated proteins in blue. Data represented as Log_2FoldChange (FC) of mean abundance of proteins normalized to iNSC Cav-1 WT (n=3 iNSC Cav-1 KO and n=3 iNSC Cav-1 WT). DEP determined by a one-way ANOVA with a p-value of < 0.05.

(C) Bar chart showing the top 10 Ingenuity Pathway Analysis (IPA) altered pathways in the iNSC Cav-1 KO compared to iNSC Cav-1 WT hippocampal NSPCs (ANOVA, $p < 0.05$).

(D) Cytoscape cluster mapping of altered GO pathways in hippocampal NSPCs isolated from iNSC Cav-1 KO and iNSC Cav-1 WT mice. Analysis based on Log_2FC ratio of DEPs with a significant cut off value of $p < 0.05$.

(E) Weighted Venn diagram depicting overlap of DEP with genes encoding proteins localizing to mitochondria based on Mitocarta 3.0 curation[51].

(F) Volcano plot and (G) Table of Mitocarta 3.0[51] proteins identified in iNSC Cav-1 KO vs iNSC Cav-1 WT cells. Metabolism related protein in orange; Protein Import, Sorting & Homeostasis in green; Signaling and Molecule Transport in blue, Mitochondria Central Dogma in purple; and Mitochondria Dynamics and Surveillance in pink.

Figure 7. Cav-1 regulates mitochondrial morphology and dynamics in hippocampal NSPC.

(A) Representative confocal image of Caveolin-1 (Cav-1, Green), Mitochondrial import receptor subunit TOM20 homolog (Tom-20, green) and DAPI (blue) immunostaining in WT hippocampal NSPCs. Scale bar 10 µm. Mander's Correlation Coefficient of co-localization of Cav-1 with Tom-20 determined with ImageJ.

(B) Immunoblot of Cav-1, Dynamin-related protein 1 (Drp-1) and Tom-20 in total cell lysate, cytosol fraction and mitochondrial enriched fraction of WT hippocampal NSPCs. Data represented as mean ± SEM.

(C) Immunoblot of Drp-1, mitofusion-2 (Mfn-2) and Tom-20 in total cell lysate (TC), cytosol fraction (Cyto) and mitochondrial enriched fraction (Mito) of iNSC Cav-1 WT and iNSC Cav-1 KO hippocampal NSPCs.

(D) Normalization of iNSC Cav-1 KO Drp-1 and Mfn-2 in cytosol enriched fraction to iNSC Cav-1 WT expression.

(E) Normalization of iNSC Cav-1 KO Drp-1 and Mfn-2 expression in mitochondrial enriched fraction to iNSC Cav-1 WT expression. Data representative of n=1 T-75 flask of NSPC per genotype.

(F) Representative transmission electron microscopy (TEM) images of NSPCs isolated from iNSC Cav-1 KO and iNSC Cav-1 WT mice. Mitochondria are shaded in green; scale bar = 1 µm with zoomed image scale bar = 500 nm.

(G) Representative live-cell images of TMRM staining in NSPCs isolated from iNSC Cav-1 KO and iNSC Cav-1 WT mice. NSPCs were incubated with 50 nM TMRM for 30 min followed by confocal microcopy visualization. Mitochondria were skeletonized in ImageJ. Scale bar, 10 µm.

(H-J) Quantification of mitochondria area per cell, mitochondria perimeter per cell, and circularity per cell in iNSC Cav-1 WT and iNSC Cav-1 KO NSCPs. N=25 cells per group.

(K) Quantification of skeletonized mitochondria branch length per mitochondria in iNSC Cav-1 WT and iNSC Cav-1 KO NSCPs. N=25 cells per group.

(L) Quantification of TMRM fluorescence in iNSC Cav-1 WT and iNSC Cav-1 KO NSPC. N=25 cells per group.

(M) Representative images of mitochondria trafficking per minute using Trackmate[60] in iNSC Cav-1 WT and iNSC Cav-1 KO NSPCs. Scale bar 10 µm.

(N) Quantification of mitochondria velocity. n=10 cells per genotype with n=948 particles (mitochondria) for iNSC Cav-1 WT and n=1259 particles (mitochondria) for iNSC Cav-1 KO analyzed.

(O) Quantification of mitochondria total distanced traveled. n=10 cells per genotype with n=948 particles (mitochondria) for iNSC Cav-1 WT and n=1259 particles (mitochondria) for iNSC Cav-1 KO analyzed.

Data represented as mean ± SEM. Data analyzed in by unpaired two-tailed Student's t-test except in (N,O) was analyzed by two-way ANOVA with Tukey's multiple comparisons correction. ns $p > 0.05$, *$p < 0.05$, **$p < 0.01$, ***$p < 0.001$ and ****$p < 0.0001$.

Methods

Mouse Models

All mouse experiments were approved by the University of Illinois at Chicago Institutional Animal Care and Use Committee. Mice were housed on a 12-hour light/dark cycle and provided food and water ad libitum. C57Bl/6J wildtype (WT) and global Cav-1 knockout (gCav-1 KO) used in experiments were from Jackson Laboratories (Strain #:000664 and Strain #: 007083, respectively). Inducible NSPC specific-Cav-1 knockout mice (NestinCre$^{ERT2/+}$;Cav-1$^{fl/fl}$) were generated by crossing NestinCre$^{ERT2/+}$ mice [2,13] with Cav-1$^{fl/fl}$ mice [40,41]. The NestinCre$^{ERT2/+}$ transgene was maintained as hemizygous and the Cav-1$^{fl/fl}$ homozygous. Male mice were used in experiments unless otherwise stated in text.

Tamoxifen Injections

Tamoxifen (TAM, Sigma-Aldrich) was dissolved in corn oil (Sigma-Aldrich) at 20 mg/mL at 37°C and then stored at 4°C for 5 days. To induce recombination, 4–5-week-old mice were intraperitoneally injected at a dose of 130 mg/kg TAM or equal volume of corn oil once a day for 5 consecutive days.

NSPC Isolation and Culture

Primary hippocampal NSPCs were isolated from 6–8-week-old mice similarly as described [43,76]. Hippocampi were dissected in ice-cold HBSS and pooled from 4-6 mice. Hippocampi were transferred to a tissue culture hood, minced using a sterile scalpel until no visible pieces remained (3-5 mins) and transferred to 3-5 mL of warm culture media (DMEM/F-12 with 20 mM KCl, 2 µg/mL heparin, 1% penicillin–streptomycin, 20% B27 supplement, 10% N2 supplement). Tissue was spun at 200g for 2 mins and dissociated with 0.1% Trypsin-EDTA (diluted in DMEM/F12) at 37°C for 10 mins. After incubation, tissue was triturated 5 times with a P1000 pipette. Next, 3 mL of trypsin-inhibitor (0.139 mg/mL and 1U/mL DNase I in HBSS-/-) was added, triturated with a P1000 pipette 5 times and centrifuged at 300g for 5 mins. The cell pellet was singly resuspended in 1 mL of culture media by pipetting an additional 25 times with a P1000 pipette followed by filtration through a 40 µm cell strainer and filter washed with 15-20 mL of culture media. Cells were centrifuged 300g for 5 mins and resuspended in 1 mL of culture media plus growth factors (20 ng/mL EGF and 10 ng/mL bFGF) by pipetting 10 times with a P1000 pipette. Cells were plated in a 24-well plate (1 well per mouse) containing 2 mL of culture media plus growth factors. Half media changes were preformed every 48 hrs for 7-10 days with growth factors added to culture media immediately prior to use.

After the first 7-10 days, cells were collected and centrifuged 300g for 5 mins. The cell pellet was singly dissociated by pipetting 20 times with a P1000 pipette in 1 mL of culture media containing growth factors. The cell suspension was filtered through a 40 µm cell strainer and filter washed with 15-20 mL of culture media. Cells were centrifuged 300g for 5 mins, resuspended in 1 mL of culture media plus growth factors and plated in 2-3 wells of 6-well plate containing 3 mL of culture media plus growth factors per well. Half media changes were preformed every 48 hrs until ~100 µm in diameter neurospheres are formed (7-10 days). All experiments were performed using NSPCs between passage numbers 3 to 8, where neurospheres were dissociated using Accutase (StemCell Technologies) at 37°C for 7 mins followed by the addition of 5 mL culture media and centrifuged 300g for 5 mins. Cells were counted and plated at 10,000 cells/cm^2 for floating neurosphere cultures. For experiments requiring monolayers, singly dissociated NSPCs were grown on poly-L-orthinine/laminin (PLO/laminin) coated plastic dishes or acid washed coverslips. Briefly, plastic dishes and coverslips were incubated at 37°C with 15 µg/mL PLO diluted in 1X PBS for 24-48 hr, washed with 1X PBS and incubated at 37°C with 10 µg/mL laminin in 1X PBS for 24 hr. PLO/laminin coated dishes or coverslips were washed 1 time with 1X PBS prior to plating of cells.

BrdU and EdU Labeling

For the 12-day *in vivo* experiments, 5-bromo-2'-deoxyuridine (BrdU, Sigma) was prepared fresh daily by dissolving BrdU at 20 mg/mL in 1X PBS at 37°C and then sterile filtered via 0.22µm syringe filter. Mice were intraperitoneally injected at a dose of 100 mg/kg once daily for 12 consecutive days and tissue collected 24 hr after the last injection. Mice were sacrificed and tissue collected 4 weeks after the last injection. For *in vitro* BrdU and EdU experiments, NSPCs were seeded on PLO/laminin coated coverslips at a density of 50,000 cells/cm^2 and incubated overnight in culture media containing growth factors. A 5 mM EdU stock was

prepared in DMSO and stored at -20°C until use. EdU stock solutions were diluted to 5 μM in culture media, sterile filtered via 0. 22μm syringe filter and growth factors added immediately prior to the start of the experiment.

Clonogenic Proliferation Assay

Hippocampal NSPCs were singly dissociated and plated as floating cultures in 96-well plates at 1000 cells per well. Cells were grown in culture media containing growth factors (20 ng/mL EGF and 10 ng/mL bFGF) and growth factors were added to media every 48 hr. On day 6, cultures were imaged using a Keyence BZ-X800 followed by dissociation with Accutase to count the number of cells per well. The number and diameter of neurospheres (clones) per well was quantified using ImageJ.

Differentiation Assay

Hippocampal NSPCs were seeded on PLO/laminin coated plastic dishes or coverslips at a density of 50,000 cells/cm^2. Cells were grown in culture media containing growth factors (20 ng/mL EGF and 10 ng/mL bFGF) overnight (8-12 hours). Media was then changed to differentiation media consisting of culture media (DMEM/F-12 with 20 mM KCl, 2 μg/mL heparin, 1% penicillin–streptomycin, 20% B27 supplement, 10% N2 supplement) with 1 μM retinoic acid (Sigma) and 5 μM forskolin (Sigma). Half of the media was changed every 48-72 hours. Cells were fixed or collected after 3 or 7 days of differentiation.

Immunohistochemistry and Immunocytochemistry

Mice were transcardially perfused with ice cold PBS followed by 4% PFA in 1X PBS. Brains were post-fixed for 24 hr in 4% PFA followed by immersion in 10% sucrose in 1X PBS for 24 hr, 20% sucrose in 1X PBS for 24 hr and 30% sucrose 1X PBS for 24 hr. Brains were sectioned at 40 μm using a sliding microtome and floating coronal sections were stored in

cryoprotectant consisting of glycerol (20% v/v) and ethylene glycol (24% v/v) in 1X PBS at -20°C. Sections were washed with 1X PBS, incubated with 1% sodium borohydride in 1X PBS for 10 mins at RT and washed 3 times with 1X PBS for 10 min per wash. For antibodies requiring heat induced antigen retrieval, sections were incubated in 10 mM sodium citrate buffer containing 0.05% Tween 20, pH 6.0 at 99°C for 15 mins in a vegetable steamer. For BrdU immunodection, sections were washed with 1X PBS, treated in pre-warmed 1N HCl for 40 min at 37°C followed by incubation with 0.1 M sodium borate buffer pH 8.5 for 10 min at RT. Following, antigen retrieval or HCl pre-treatment, sections were washed 3 times with 1X PBS for 10 min per wash. Sections were blocked in 1X PBS containing 0.3 M Glycine, 0.2% Triton X-100 and 5% normal donkey serum (NDS) for 1 hr at RT. After blocking, sections were incubated with primary antibodies diluted in block solution for 48 hr at 4°C. After primary incubation, sections were washed 3 times in PBS containing 0.1% Tween-20 (PBST) for 15 mins per wash. Sections were incubated with secondary antibodies diluted in block solution for 1.5-2 hr at RT. Sections were washed 3 times in PBST for 15 mins per wash, counterstained with DAPI, and mounted on Superfrost Plus slides (ThermoFisher) with Prolong Gold Antifade Mountant (Invitrogen).

For immunocytochemistry (ICC), culture media was removed, coverslips containing cells were washed two times with 1X PBS and fixed in 4% PFA in 1X PBS for 20 min at RT. Cells were washed two times with 1X PBS and blocked in 1X PBS containing 0.3 M Glycine, 0.2% Triton X-100 and 5% NDS for 30 minutes at RT. For EdU detection, cells were processed according to the Click-iT EdU Cell Proliferation Kit (Invitrogen) instructions prior to blocking step. For BrdU immunodection, cells were treated in pre-warmed 1N HCl for 40 min at 37°C followed by incubation with 0.1 M sodium borate buffer pH 8.5 for 10 min at RT prior to blocking step. Primary antibodies were diluted in blocking solution and incubated 24 hr at 4°C. After primary incubation, cells were washed 3 times in PBST for 5 mins per wash and incubated with

secondary antibodies diluted in blocking solution for 45 min at RT. Cells were then washed 3 times in PBST for 5 mins per wash, counterstained with DAPI and mounted with Prolong Gold Antifade Mountant (Invitrogen). All antibodies used in experiments are listed in Key Resource Table. Images were acquired at 40x or 63x magnification using confocal microscopy (Zeiss LSM 710).

Transmission Electron Microscopy

Cells were washed 3 times with 1X PBS and centrifuged at 300g for 5 min to form pellets. Cell pellets were fixed in 1.6% glutaraldehyde in 100 mM sodium phosphate, pH 7.4 for 1 hr at room temperature as similarly described[77]. Samples were post-fixed with 1% osmium tetroxide for 1 hr and dehydrated using an ascending series of ethanol (through 100% absolute). Sample were then embedded in LX112 epoxy resin and polymerized at 60°C for 3 days. Ultrathin sections (~75 nm) were collected onto copper grids and stained with uranyl acetate and lead citrate, respectively. Specimens were examined using a JEOL JEM-1400F transmission electron microscope at 80 kV. Micrographs were acquired using an AMT Side-Mount Nano Sprint Model 1200S-B and Biosprint 12M-B cameras, loaded with AMT Imaging software V.7.0.1.

RNA Isolation

To isolate RNA, cells were washed 2 times with 1X PBS and RNA was isolated using a RNAeasy Plus Mini Kit (Qiagen).

Quantitative Real-Time PCR

Quantitative real-time PCR (qRT-PCR) was used to measure RNA with Luna Universal One-Step RT-qPCR Kit (New England Biolabs) via CFX Connect Real-Time PCR Detection

System (Bio-Rad). Target gene expression was normalized to gene expression of GAPDH or β-Actin.

Western blotting

Cells were washed 3 times with 1X PBS and lysed on ice for 10 mins in RIPA buffer containing protease and phosphatase inhibitor cocktails (ThermoFisher). Lysed samples were sonicated on ice at 20% power 3 times for 15 s with 5 s rest between sonication. Samples were centrifuges at 10,000g for 15 mins to remove insoluble material and cellular debris. The supernatant was collected and protein concentration determined by BCA Protein Assay Kit (ThermoFisher). Samples were prepared in sample buffer consisting of NuPAGE LDS Sample Buffer and NuPAGE reducing agent followed by boiling for 5 mins at 95°C. Protein were separated on Bolt Bis-Tris Plus SDS-PAGE gels (Invitrogen) with MES SDS running buffer (Invitorgen) and transferred to 0.2 µm nitrocellulose membranes via the iBlot 2 Dry Blotting System (Invitrogen) Membranes were blocked for 1 hr at RT in 5% non-fat dry milk (milk) diluted in TBS containing 0.1% Tween-20 (TBST). Primary antibodies were diluted in 5% milk in TBST and membranes incubated overnight at 4°C. Membranes were washed 3 times for 15 mins per wash with TBST followed by incubation with HRP conjugated secondary antibodies diluted in 5% milk in TBST for 2 hr at RT. Membranes were washed 3 times for 15 mins per wash and developed with ECL Super Signal Kit via Kodak RP X-OMAT developer or Azure Biosystems 300q Image Western Blot Imaging System. Band intensities were quantified in Fiji (NIH) from scanned images and total protein expression was normalized to GAPDH or β-Actin protein expression.

Cell Quantification

For *in vivo* experiments, every sixth section of brain tissue was quantified using unbiased stereology (StereoInvestigator, MBF Biosciences). Under the optical fractionator workflow, contours of the DG were traced under 10x magnification and cells counted under 63x magnification. A 120 µm x 120 µm counting frame with a 2 µm guard zone on both sides of the section and a counting grid size determined by sampling 35% or 50% of the contour was used. The volume of DG (μm^3) was determined by multiplying the area of contour by the measured mounted thickness of the section. Total cell counts were normalized to volume of DG (μm^3) counted per mouse. Alternatively for DCX and NeuN cell quantification, 30 µm z-stacks of the DG were acquired at 25x magnification using confocal microscopy (Zeiss LSM 710) and positive cells counted from maximum projection images in Fiji (NIH). For in vitro experiments, 10 µm z-stacks were acquired at 40x or 63x magnification using confocal microscopy (Zeiss LSM 710) and positive cells counted from maximum projection images in Fiji (NIH).

Behavior Tests

All mice were handled 3-5 days for 2 min per mouse per day prior to the start of behavior testing.

Elevated Plus Maze

The elevated plus maze (EPM) test was used to examine anxiety-like behavior. The EPM apparatus consisted of two open arms without walls and two closed arms with opaque walls. Mice were placed at the center of the apparatus facing an open arm and allowed to freely explore for 5 mins. The EPM apparatus was cleaned with 70% ethanol between mice. Video recordings were analyzed by Ethovision XT v16 software (Noldus) and the time spent in the open and closed arms as well as frequency of entries into the arms was calculated.

Novel Object Location

The novel object location (NOL) test was used to examine spatial learning and memory behavior as similarly described in X. A 38 cm x 51 cm x 30 cm opaque white plastic chamber box with one short end containing a black circle wall print and the other short end containing a black vertical line wall print was utilized. On day 1 of the test, mice were habituated in the empty box for 10 mins followed by placement of 2 identical objects equal distance a part on the short end of the box containing the black circle wall print for 10 mins. Objects were removed for 5 min and then replaced in same locations for another 10 min session. Mice were placed back in home cages for 24 hrs. On day 2, mice were habituated in the empty box for 10 mins and tested by placing one of the objects in a novel location diagonally to the other one along the short end of the box with black vertical line wall print. Mice were allowed to explore the objects for 5 mins. Video was captured for every trial and exploration time with each object was manually scored blinded. Chambers were cleaned with 70% ethanol between mice. The discrimination index (DI) was calculated as $DI = (T_N-T_o)/(T_n+T_o)$, where T_N is the exploration time with the object in the new location and T_o the exploration time with the object in the old location.

Contextual Fear Discrimination

This contextual fear discrimination test was conducted similarly as described[47]. All contexts consisted of 17.8 cm x 17.8 cm x 30.5 cm chamber housed in a sound isolation cubicle (Coulbourn Instruments). Context A consisted of two translucent plexiglass walls, two walls comprised of alternating black and white metal tiles and a stainless-steel rod floor. Context A also had a 28V exhaust fan. Context B had no fan and consisted of two walls comprised of alternating black and white metal tiles, two walls of black vertical line print and a stainless-steel rod floor. To test fear generalization, Context B was exchanged with Context C that had no fan, a circular wall insert made of up of a black and white plastic sheet and a black plastic floor covering. On day 1 of the test, mice were exposed to Context A for 10 mins. On day 2, mice were placed in Context A, received a 2s foot shock (0.7mA) immediately upon entry and

remained in Context A for an additional 28s (a total of 30s in Context A). Thirty mins later, mice were placed back in Context A for a 3 min exposure trial followed by placement in Context B for 3 min exposure trial. On day 3 (24 hr post-shock), mice were placed in Context A for 3 mins or Context B for 3 mins in a counter-balanced order. For a less difficult discrimination test, mice followed the same sequence as stated but were placed in Context C instead of Context B on day 2 and 3. FreezeFrame software (Actimetrics) was used for video recording and analysis of freezing behavior in each context. Chamber walls and floor were cleaned with 70% ethanol between mice. The discrimination index (DI) was calculated as DI = $(F_A-F_x)/(F_A+F_x)$, where F_A is the percentage of freezing in Context A and F_x is the percentage of freezing in either Context B or Context C.

Nano-LC-MS/MS analysis

Cells were isolated as described in Section 2.2.4 and washed 3 times in 1X PBS prior to freezing in liquid nitrogen. Cell pellets were lysed in 10% sodium dodecyl sulfate (SDS) containing 100 mM triethylammonium bicarbonate (TEAB) with Pierce protease inhibitor (ThermoFisher Scientific) supplemented, sonicated, and centrifuged at 14,000 rpm for 10 minutes. Protein supernatant was collected and quantified using a BCA Protein Assay Kit (ThermoFisher). 100 ug of protein per sample was processed, trypsin digested in S-Trap microcolumns (Protifi), and peptides labeled according to the TMT10plex Isobaric Label Reagent Set (ThermoFisher) manufacture instructions. 100 fmol green fluorescent protein (GFP) per µg of protein was spiked in each sample before digestion. Each individual isobaric labeled sample was combined, lyophilized, and resuspended in 10 mM ammonium hydroxide prior to fractionation by high pH reversed-phase liquid chromatography. 60 fractions were collected and further concatenated into 20 fractions by combining 3 fractions for every 20 fractions apart[78]. All fractions were dried down completely then resuspended in 0.1% formic acid. Peptide chromatographic separations and mass detection occurred with an Agilent 1260

nano/capillary HPLC system (Agilent Technologies) coupled to an Q-Exactive Orbitrap mass spectrometer (MS, ThermoFisher Scientific). Peptides were loaded onto an Acclaim PepMap 100 trap column (75 µm × 2 cm nanoViper, C18, 3 µm 100 Å, ThermoFisher Scientific) at flow rate of 2 µL/min. Peptides were further separated using a Zorbax 300SB-C18 column (0.075×150 mm, 3.5 µm 300 Å) (Agilent Technologies) at a flow rate of 0.25 µL/min, and eluted using a 5-30% mobile phase B gradient consisting of 0.1% formic acid in acetonitrile over 90 minutes. Data was collected in the data-dependent acquisition (DDA) mode at a mass resolution of 70,000 and scan range 375-2000 m/z. Automatic gain control (AGC) target was set at 1×10^6 for a maximum injection time (IT) of 100 ms. The top 10 most abundant precursors (charge state between 2 and 5) were selected for MS/MS analysis. MS/MS spectra were acquired at a resolution of 35,000, AGC target at 1×10^6, and maximum IT of 50 ms. All raw mass spectrometry data is publicly available on MassIVE with project ID MSV000090289 (ftp://massive.ucsd.edu/MSV000090289/).

The raw MS/MS data for each sample was searched against the curated SwissProt *Mus musculus* database in Proteome Discoverer software (v2.3.0.523, ThermoFisher Scientific), where trypsin was selected as the protease with 2 or less missed cleavage sites, precursor and fragment mass error tolerances set to 10 ppm and ± 0.02 Da, and only peptide precursors of +2, +3, +4 were analyzed. Peptide variable modifications allowed during the search were: oxidation ((+15.995 Da; M), TMT6 (+229.163 Da; S, T), and acetylation (+42.011 Da; N-terminus), whereas carbamidomethyl (+57.021 Da; C) and TMT (+229.163 Da; any N-terminus) were set as static modifications. Samples were grouped as iNSC Cav-1 KO (n=3) and iNSC Cav-1 WT (n=3). Protein identifications were accepted if they contained at least 2 unique peptides and abundances normalized to total peptide abundance. Differentially expressed proteins (DEP) for the iNSC Cav-1 KO NSPCs relative to the iNSC Cav-1 WT NSPCs were determined by applying ANOVA with a p-value of < 0.05.

Protein pathway and mitochondria protein analysis

Protein pathway analysis was conducted on DEP using Ingenuity Pathway Analysis (IPA, Qiagen) and Gene Ontology (GO) enrichment analysis[77,79] using g:Profiler[80] (ve107_eg54_p17_bf42210). Functional enrichment maps were constructed in Cytoscape[81] with EnrichmentMap pipeline collection applications[82]. Mitochondria pathways and functional groups were determined by manual curation using the MitoCarta 3.0 dataset[51].

Mitochondria Isolation

Cells were washed 3 times with 1X PBS and mitochondria were isolated according to the manufacturer instructions using the Mitochondria Isolation Kit (ThermoFisher). Briefly, cells were pelleted by centrifugation at 300g for 5 mins at 4°C. Reagent A containing protease and phosphatase inhibitor cocktails (ThermoFisher) was added to the cell pellet and placed on ice for 2 mins. Cells were then lysed by 100 strokes using a Dounce tissue homogenizer. Following the addition of Reagent C, the lysate was centrifuged at 700g for 10 mins at 4°C. The supernatant was then collected and centrifuged at 3000g for 15 min at 4°C to pellet mitochondria from the cytosol. The cytosol containing supernatant was collected and the mitochondria enriched pellet was washed with Reagent C and then centrifuged for 12000g for 5 mins at 4°C. The mitochondria enriched pellet was lysed in 1% CHAPS in TBS and processed for BCA protein estimation and western blotting as described.

TMRM Live Cell Imaging

Tetramethylrhodamine, methyl ester (TMRM) live cell imaging was conducted similarly as described[83]. Singly dissociated NSPCs were grown on PLO/laminin coated 35mm glass bottom live cell imaging dishes at a density of 50,000 cells/well. 24 hrs after plating, media was replaced with proliferation media containing 50 nM TMRM. Cells were incubated with TMRM for 30 mins at 37°C. Immediately prior to imaging, cells were washed 2 times with PBS followed by

replacement of proliferation media lacking phenol red. 2D images were captured with a 63X objective using a Zeiss LSM880 META confocal microscope with heated stage and a DPSS 561-10 laser set at 0.1% laser power with GaAsP detection. For quantification of mitochondria morphology, images were analyzed with ImageJ as described[84]. For 2D time lapse videos, images were captured with 3x digital zoom for 120 s at frame rate of 3 Hz. Mitochondria velocity and total distance traveled were measured using the Trackmate[60] plugin in ImageJ.

Statistics

In all graphs, data is shown as mean ± SEM. Prism (Graphpad) was used for statistical analysis with tests indicated in figure legends. The following was used for p values: ns > 0.05, *p < 0.05, **p < 0.01, ***p < 0.001, and ****p < 0.0001.

References

1. Toda, T., Parylak, S.L., Linker, S.B., and Gage, F.H. (2019). The role of adult hippocampal neurogenesis in brain health and disease. Mol Psychiatry *24*, 67-87. 10.1038/s41380-018-0036-2.
2. Sahay, A., Scobie, K.N., Hill, A.S., O'Carroll, C.M., Kheirbek, M.A., Burghardt, N.S., Fenton, A.A., Dranovsky, A., and Hen, R. (2011). Increasing adult hippocampal neurogenesis is sufficient to improve pattern separation. Nature *472*, 466-470. 10.1038/nature09817.
3. Miller, S.M., and Sahay, A. (2019). Functions of adult-born neurons in hippocampal memory interference and indexing. Nat Neurosci *22*, 1565-1575. 10.1038/s41593-019-0484-2.
4. Niibori, Y., Yu, T.S., Epp, J.R., Akers, K.G., Josselyn, S.A., and Frankland, P.W. (2012). Suppression of adult neurogenesis impairs population coding of similar contexts in hippocampal CA3 region. Nat Commun *3*, 1253. 10.1038/ncomms2261.

5. Masachs, N., Charrier, V., Farrugia, F., Lemaire, V., Blin, N., Mazier, W., Tronel, S., Montaron, M.F., Ge, S., Marsicano, G., et al. (2021). The temporal origin of dentate granule neurons dictates their role in spatial memory. Mol Psychiatry *26*, 7130-7140. 10.1038/s41380-021-01276-x.

6. Britton, R., Liu, A.T., Rege, S.V., Adams, J.M., Akrapongpisak, L., Le, D., Alcantara-Lee, R., Estrada, R.A., Ray, R., Ahadi, S., et al. (2022). Molecular and histological correlates of cognitive decline across age in male C57BL/6J mice. Brain Behav *12*, e2736. 10.1002/brb3.2736.

7. Encinas, J.M., Michurina, T.V., Peunova, N., Park, J.H., Tordo, J., Peterson, D.A., Fishell, G., Koulakov, A., and Enikolopov, G. (2011). Division-coupled astrocytic differentiation and age-related depletion of neural stem cells in the adult hippocampus. Cell Stem Cell *8*, 566-579. 10.1016/j.stem.2011.03.010.

8. Demars, M.P., Hollands, C., Zhao Kda, T., and Lazarov, O. (2013). Soluble amyloid precursor protein-alpha rescues age-linked decline in neural progenitor cell proliferation. Neurobiol Aging *34*, 2431-2440. 10.1016/j.neurobiolaging.2013.04.016.

9. Terreros-Roncal, J., Moreno-Jimenez, E.P., Flor-Garcia, M., Rodriguez-Moreno, C.B., Trinchero, M.F., Cafini, F., Rabano, A., and Llorens-Martin, M. (2021). Impact of neurodegenerative diseases on human adult hippocampal neurogenesis. Science *374*, 1106-1113. 10.1126/science.abl5163.

10. Moreno-Jimenez, E.P., Flor-Garcia, M., Terreros-Roncal, J., Rabano, A., Cafini, F., Pallas-Bazarra, N., Avila, J., and Llorens-Martin, M. (2019). Adult hippocampal neurogenesis is abundant in neurologically healthy subjects and drops sharply in patients with Alzheimer's disease. Nat Med *25*, 554-560. 10.1038/s41591-019-0375-9.

11. Tobin, M.K., Musaraca, K., Disouky, A., Shetti, A., Bheri, A., Honer, W.G., Kim, N., Dawe, R.J., Bennett, D.A., Arfanakis, K., and Lazarov, O. (2019). Human Hippocampal

Neurogenesis Persists in Aged Adults and Alzheimer's Disease Patients. Cell Stem Cell *24*, 974-982 e973. 10.1016/j.stem.2019.05.003.

12. Demars, M., Hu, Y.S., Gadadhar, A., and Lazarov, O. (2010). Impaired neurogenesis is an early event in the etiology of familial Alzheimer's disease in transgenic mice. J Neurosci Res *88*, 2103-2117. 10.1002/jnr.22387.

13. Mishra, R., Phan, T., Kumar, P., Morrissey, Z., Gupta, M., Hollands, C., Shetti, A., Lopez, K.L., Maienschein-Cline, M., Suh, H., et al. (2022). Augmenting neurogenesis rescues memory impairments in Alzheimer's disease by restoring the memory-storing neurons. J Exp Med *219*. 10.1084/jem.20220391.

14. Choi, S.H., Bylykbashi, E., Chatila, Z.K., Lee, S.W., Pulli, B., Clemenson, G.D., Kim, E., Rompala, A., Oram, M.K., Asselin, C., et al. (2018). Combined adult neurogenesis and BDNF mimic exercise effects on cognition in an Alzheimer's mouse model. Science *361*. 10.1126/science.aan8821.

15. Hu, Y.S., Xu, P., Pigino, G., Brady, S.T., Larson, J., and Lazarov, O. (2010). Complex environment experience rescues impaired neurogenesis, enhances synaptic plasticity, and attenuates neuropathology in familial Alzheimer's disease-linked APPswe/PS1DeltaE9 mice. FASEB J *24*, 1667-1681. 10.1096/fj.09-136945.

16. Zhou, Y., Su, Y., Li, S., Kennedy, B.C., Zhang, D.Y., Bond, A.M., Sun, Y., Jacob, F., Lu, L., Hu, P., et al. (2022). Molecular landscapes of human hippocampal immature neurons across lifespan. Nature *607*, 527-533. 10.1038/s41586-022-04912-w.

17. Artegiani, B., Lyubimova, A., Muraro, M., van Es, J.H., van Oudenaarden, A., and Clevers, H. (2017). A Single-Cell RNA Sequencing Study Reveals Cellular and Molecular Dynamics of the Hippocampal Neurogenic Niche. Cell Rep *21*, 3271-3284. 10.1016/j.celrep.2017.11.050.

18. Vicidomini, C., Guo, N., and Sahay, A. (2020). Communication, Cross Talk, and Signal Integration in the Adult Hippocampal Neurogenic Niche. Neuron *105*, 220-235. 10.1016/j.neuron.2019.11.029.

19. Gadadhar, A., Marr, R., and Lazarov, O. (2011). Presenilin-1 regulates neural progenitor cell differentiation in the adult brain. J Neurosci *31*, 2615-2623. 10.1523/JNEUROSCI.4767-10.2011.

20. Demars, M.P., Bartholomew, A., Strakova, Z., and Lazarov, O. (2011). Soluble amyloid precursor protein: a novel proliferation factor of adult progenitor cells of ectodermal and mesodermal origin. Stem Cell Res Ther *2*, 36. 10.1186/scrt77.

21. Williams, T.M., and Lisanti, M.P. (2004). The caveolin proteins. Genome Biol *5*, 214. 10.1186/gb-2004-5-3-214.

22. Parton, R.G. (2018). Caveolae: Structure, Function, and Relationship to Disease. Annu Rev Cell Dev Biol *34*, 111-136. 10.1146/annurev-cellbio-100617-062737.

23. Parton, R.G., McMahon, K.A., and Wu, Y. (2020). Caveolae: Formation, dynamics, and function. Curr Opin Cell Biol *65*, 8-16. 10.1016/j.ceb.2020.02.001.

24. Ikezu, T., Ueda, H., Trapp, B.D., Nishiyama, K., Sha, J.F., Volonte, D., Galbiati, F., Byrd, A.L., Bassell, G., Serizawa, H., et al. (1998). Affinity-purification and characterization of caveolins from the brain: differential expression of caveolin-1, -2, and -3 in brain endothelial and astroglial cell types. Brain Res *804*, 177-192. 10.1016/s0006-8993(98)00498-3.

25. Virgintino, D., Robertson, D., Errede, M., Benagiano, V., Tauer, U., Roncali, L., and Bertossi, M. (2002). Expression of caveolin-1 in human brain microvessels. Neuroscience *115*, 145-152. 10.1016/s0306-4522(02)00374-3.

26. Blochet, C., Buscemi, L., Clement, T., Gehri, S., Badaut, J., and Hirt, L. (2020). Involvement of caveolin-1 in neurovascular unit remodeling after stroke: Effects on

neovascularization and astrogliosis. J Cereb Blood Flow Metab *40*, 163-176. 10.1177/0271678X18806893.

27. Filchenko, I., Blochet, C., Buscemi, L., Price, M., Badaut, J., and Hirt, L. (2020). Caveolin-1 Regulates Perivascular Aquaporin-4 Expression After Cerebral Ischemia. Front Cell Dev Biol *8*, 371. 10.3389/fcell.2020.00371.

28. Knowland, D., Arac, A., Sekiguchi, K.J., Hsu, M., Lutz, S.E., Perrino, J., Steinberg, G.K., Barres, B.A., Nimmerjahn, A., and Agalliu, D. (2014). Stepwise recruitment of transcellular and paracellular pathways underlies blood-brain barrier breakdown in stroke. Neuron *82*, 603-617. 10.1016/j.neuron.2014.03.003.

29. Chow, B.W., Nunez, V., Kaplan, L., Granger, A.J., Bistrong, K., Zucker, H.L., Kumar, P., Sabatini, B.L., and Gu, C. (2020). Caveolae in CNS arterioles mediate neurovascular coupling. Nature *579*, 106-110. 10.1038/s41586-020-2026-1.

30. Bonds, J.A., Shetti, A., Bheri, A., Chen, Z., Disoukey, A., Tai, L., Mao, M., Head, B.P., Bonini, M.G., Haus, J.M., et al. (2019). Depletion of Caveolin-1 in Type-2 Diabetes Model Induces Alzheimer's disease Pathology Precursors. J Neurosci. 10.1523/JNEUROSCI.0730-19.2019.

31. Trushina, E., Du Charme, J., Parisi, J., and McMurray, C.T. (2006). Neurological abnormalities in caveolin-1 knock out mice. Behav Brain Res *172*, 24-32. 10.1016/j.bbr.2006.04.024.

32. Gioiosa, L., Raggi, C., Ricceri, L., Jasmin, J.F., Frank, P.G., Capozza, F., Lisanti, M.P., Alleva, E., Sargiacomo, M., and Laviola, G. (2008). Altered emotionality, spatial memory and cholinergic function in caveolin-1 knock-out mice. Behav Brain Res *188*, 255-262. 10.1016/j.bbr.2007.11.002.

33. Head, B.P., Peart, J.N., Panneerselvam, M., Yokoyama, T., Pearn, M.L., Niesman, I.R., Bonds, J.A., Schilling, J.M., Miyanohara, A., Headrick, J., et al. (2010). Loss of caveolin-

1 accelerates neurodegeneration and aging. PLoS One *5*, e15697. 10.1371/journal.pone.0015697.

34. Head, B.P., Hu, Y., Finley, J.C., Saldana, M.D., Bonds, J.A., Miyanohara, A., Niesman, I.R., Ali, S.S., Murray, F., Insel, P.A., et al. (2011). Neuron-targeted caveolin-1 protein enhances signaling and promotes arborization of primary neurons. J Biol Chem *286*, 33310-33321. 10.1074/jbc.M111.255976.

35. Egawa, J., Zemljic-Harpf, A., Mandyam, C.D., Niesman, I.R., Lysenko, L.V., Kleschevnikov, A.M., Roth, D.M., Patel, H.H., Patel, P.M., and Head, B.P. (2018). Neuron-Targeted Caveolin-1 Promotes Ultrastructural and Functional Hippocampal Synaptic Plasticity. Cereb Cortex *28*, 3255-3266. 10.1093/cercor/bhx196.

36. Shikanai, M., Nishimura, Y.V., Sakurai, M., Nabeshima, Y.I., Yuzaki, M., and Kawauchi, T. (2018). Caveolin-1 Promotes Early Neuronal Maturation via Caveolae-Independent Trafficking of N-Cadherin and L1. iScience *7*, 53-67. 10.1016/j.isci.2018.08.014.

37. Wang, S., Zhang, Z., Almenar-Queralt, A., Leem, J., DerMardirossian, C., Roth, D.M., Patel, P.M., Patel, H.H., and Head, B.P. (2019). Caveolin-1 Phosphorylation Is Essential for Axonal Growth of Human Neurons Derived From iPSCs. Front Cell Neurosci *13*, 324. 10.3389/fncel.2019.00324.

38. Frederiksen, K., and McKay, R.D. (1988). Proliferation and differentiation of rat neuroepithelial precursor cells in vivo. J Neurosci *8*, 1144-1151.

39. Wilhelmsson, U., Lebkuechner, I., Leke, R., Marasek, P., Yang, X., Antfolk, D., Chen, M., Mohseni, P., Lasic, E., Bobnar, S.T., et al. (2019). Nestin Regulates Neurogenesis in Mice Through Notch Signaling From Astrocytes to Neural Stem Cells. Cereb Cortex *29*, 4050-4066. 10.1093/cercor/bhy284.

40. Oliveira, S.D.S., Castellon, M., Chen, J., Bonini, M.G., Gu, X., Elliott, M.H., Machado, R.F., and Minshall, R.D. (2017). Inflammation-induced caveolin-1 and BMPRII depletion

promotes endothelial dysfunction and TGF-beta-driven pulmonary vascular remodeling. Am J Physiol Lung Cell Mol Physiol *312*, L760-L771. 10.1152/ajplung.00484.2016.

41. Cao, G., Yang, G., Timme, T.L., Saika, T., Truong, L.D., Satoh, T., Goltsov, A., Park, S.H., Men, T., Kusaka, N., et al. (2003). Disruption of the caveolin-1 gene impairs renal calcium reabsorption and leads to hypercalciuria and urolithiasis. Am J Pathol *162*, 1241-1248. 10.1016/S0002-9440(10)63920-X.

42. Pereira, P.D., Serra-Caetano, A., Cabrita, M., Bekman, E., Braga, J., Rino, J., Santus, R., Filipe, P.L., Sousa, A.E., and Ferreira, J.A. (2017). Quantification of cell cycle kinetics by EdU (5-ethynyl-2'-deoxyuridine)-coupled-fluorescence-intensity analysis. Oncotarget *8*, 40514-40532. 10.18632/oncotarget.17121.

43. Ahmed, A., Isaksen, T.J., and Yamashita, T. (2021). Protocol for mouse adult neural stem cell isolation and culture. STAR Protoc *2*, 100522. 10.1016/j.xpro.2021.100522.

44. Palmer, T.D., Takahashi, J., and Gage, F.H. (1997). The adult rat hippocampus contains primordial neural stem cells. Mol Cell Neurosci *8*, 389-404. 10.1006/mcne.1996.0595.

45. Clelland, C.D., Choi, M., Romberg, C., Clemenson, G.D., Jr., Fragniere, A., Tyers, P., Jessberger, S., Saksida, L.M., Barker, R.A., Gage, F.H., and Bussey, T.J. (2009). A functional role for adult hippocampal neurogenesis in spatial pattern separation. Science *325*, 210-213. 10.1126/science.1173215.

46. Nakashiba, T., Cushman, J.D., Pelkey, K.A., Renaudineau, S., Buhl, D.L., McHugh, T.J., Rodriguez Barrera, V., Chittajallu, R., Iwamoto, K.S., McBain, C.J., et al. (2012). Young dentate granule cells mediate pattern separation, whereas old granule cells facilitate pattern completion. Cell *149*, 188-201. 10.1016/j.cell.2012.01.046.

47. Clemenson, G.D., Lee, S.W., Deng, W., Barrera, V.R., Iwamoto, K.S., Fanselow, M.S., and Gage, F.H. (2014). Enrichment rescues contextual discrimination deficit associated with immediate shock. Hippocampus *25*, 385-392. 10.1002/hipo.22380 PMID - 25330953.

48. Huckleberry, K.A., Ferguson, L.B., and Drew, M.R. (2016). Behavioral mechanisms of context fear generalization in mice. Learn Mem *23*, 703-709. 10.1101/lm.042374.116.

49. Gonzalez, F., Quinn, J.J., and Fanselow, M.S. (2003). Differential effects of adding and removing components of a context on the generalization of conditional freezing. J Exp Psychol Anim Behav Process *29*, 78-83.

50. Guo, N., Soden, M.E., Herber, C., Kim, M.T., Besnard, A., Lin, P., Ma, X., Cepko, C.L., Zweifel, L.S., and Sahay, A. (2018). Dentate granule cell recruitment of feedforward inhibition governs engram maintenance and remote memory generalization. Nat Med *24*, 438-449. 10.1038/nm.4491.

51. Rath, S., Sharma, R., Gupta, R., Ast, T., Chan, C., Durham, T.J., Goodman, R.P., Grabarek, Z., Haas, M.E., Hung, W.H.W., et al. (2021). MitoCarta3.0: an updated mitochondrial proteome now with sub-organelle localization and pathway annotations. Nucleic Acids Res *49*, D1541-D1547. 10.1093/nar/gkaa1011.

52. Saotome, M., Safiulina, D., Szabadkai, G., Das, S., Fransson, A., Aspenstrom, P., Rizzuto, R., and Hajnoczky, G. (2008). Bidirectional Ca2+-dependent control of mitochondrial dynamics by the Miro GTPase. Proc Natl Acad Sci U S A *105*, 20728-20733. 10.1073/pnas.0808953105.

53. Ruggiero, A., Aloni, E., Korkotian, E., Zaltsman, Y., Oni-Biton, E., Kuperman, Y., Tsoory, M., Shachnai, L., Levin-Zaidman, S., Brenner, O., et al. (2017). Loss of forebrain MTCH2 decreases mitochondria motility and calcium handling and impairs hippocampal-dependent cognitive functions. Sci Rep *7*, 44401. 10.1038/srep44401.

54. Misko, A., Jiang, S., Wegorzewska, I., Milbrandt, J., and Baloh, R.H. (2010). Mitofusin 2 is necessary for transport of axonal mitochondria and interacts with the Miro/Milton complex. J Neurosci *30*, 4232-4240. 10.1523/JNEUROSCI.6248-09.2010.

55. Wai, T., and Langer, T. (2016). Mitochondrial Dynamics and Metabolic Regulation. Trends Endocrinol Metab *27*, 105-117. 10.1016/j.tem.2015.12.001.

56. Khacho, M., Clark, A., Svoboda, D.S., Azzi, J., MacLaurin, J.G., Meghaizel, C., Sesaki, H., Lagace, D.C., Germain, M., Harper, M.E., et al. (2016). Mitochondrial Dynamics Impacts Stem Cell Identity and Fate Decisions by Regulating a Nuclear Transcriptional Program. Cell Stem Cell *19*, 232-247. 10.1016/j.stem.2016.04.015.

57. Patel, H.H., and Insel, P.A. (2009). Lipid rafts and caveolae and their role in compartmentation of redox signaling. Antioxid Redox Signal *11*, 1357-1372. 10.1089/ars.2008.2365.

58. Fridolfsson, H.N., Kawaraguchi, Y., Ali, S.S., Panneerselvam, M., Niesman, I.R., Finley, J.C., Kellerhals, S.E., Migita, M.Y., Okada, H., Moreno, A.L., et al. (2012). Mitochondria-localized caveolin in adaptation to cellular stress and injury. FASEB J *26*, 4637-4649. 10.1096/fj.12-215798.

59. Tilokani, L., Nagashima, S., Paupe, V., and Prudent, J. (2018). Mitochondrial dynamics: overview of molecular mechanisms. Essays Biochem *62*, 341-360. 10.1042/EBC20170104.

60. Ershov, D., Phan, M.S., Pylvanainen, J.W., Rigaud, S.U., Le Blanc, L., Charles-Orszag, A., Conway, J.R.W., Laine, R.F., Roy, N.H., Bonazzi, D., et al. (2022). TrackMate 7: integrating state-of-the-art segmentation algorithms into tracking pipelines. Nat Methods *19*, 829-832. 10.1038/s41592-022-01507-1.

61. Khacho, M., and Slack, R.S. (2018). Mitochondrial dynamics in the regulation of neurogenesis: From development to the adult brain. Dev Dyn *247*, 47-53. 10.1002/dvdy.24538.

62. Urban, N., Blomfield, I.M., and Guillemot, F. (2019). Quiescence of Adult Mammalian Neural Stem Cells: A Highly Regulated Rest. Neuron *104*, 834-848. 10.1016/j.neuron.2019.09.026.

63. So, W.K., and Cheung, T.H. (2018). Molecular Regulation of Cellular Quiescence: A Perspective from Adult Stem Cells and Its Niches. Methods Mol Biol *1686*, 1-25. 10.1007/978-1-4939-7371-2_1.

64. Galbiati, F., Volonte, D., Liu, J., Capozza, F., Frank, P.G., Zhu, L., Pestell, R.G., and Lisanti, M.P. (2001). Caveolin-1 expression negatively regulates cell cycle progression by inducing G(0)/G(1) arrest via a p53/p21(WAF1/Cip1)-dependent mechanism. Mol Biol Cell *12*, 2229-2244. 10.1091/mbc.12.8.2229.

65. Wang, R., Li, Z., Guo, H., Shi, W., Xin, Y., Chang, W., and Huang, T. (2014). Caveolin 1 knockdown inhibits the proliferation, migration and invasion of human breast cancer BT474 cells. Mol Med Rep *9*, 1723-1728. 10.3892/mmr.2014.2018.

66. Bai, L., Shi, G., Zhang, L., Guan, F., Ma, Y., Li, Q., Cong, Y.S., and Zhang, L. (2014). Cav-1 deletion impaired hematopoietic stem cell function. Cell Death Dis *5*, e1140. 10.1038/cddis.2014.105.

67. Bond, A.M., Peng, C.Y., Meyers, E.A., McGuire, T., Ewaleifoh, O., and Kessler, J.A. (2014). BMP signaling regulates the tempo of adult hippocampal progenitor maturation at multiple stages of the lineage. Stem Cells *32*, 2201-2214. 10.1002/stem.1688.

68. Deng, W., Mayford, M., and Gage, F.H. (2013). Selection of distinct populations of dentate granule cells in response to inputs as a mechanism for pattern separation in mice. Elife *2*, e00312. 10.7554/eLife.00312.

69. Coelho, P., Fao, L., Mota, S., and Rego, A.C. (2022). Mitochondrial function and dynamics in neural stem cells and neurogenesis: Implications for neurodegenerative diseases. Ageing Res Rev *80*, 101667. 10.1016/j.arr.2022.101667.

70. Beckervordersandforth, R., Ebert, B., Schaffner, I., Moss, J., Fiebig, C., Shin, J., Moore, D.L., Ghosh, L., Trinchero, M.F., Stockburger, C., et al. (2017). Role of Mitochondrial Metabolism in the Control of Early Lineage Progression and Aging Phenotypes in Adult Hippocampal Neurogenesis. Neuron *93*, 560-573 e566. 10.1016/j.neuron.2016.12.017.

71. Zheng, X., Boyer, L., Jin, M., Mertens, J., Kim, Y., Ma, L., Ma, L., Hamm, M., Gage, F.H., and Hunter, T. (2016). Metabolic reprogramming during neuronal differentiation from aerobic glycolysis to neuronal oxidative phosphorylation. Elife *5*. 10.7554/eLife.13374.

72. Zhang, J., Uchiyama, J., Imami, K., Ishihama, Y., Kageyama, R., and Kobayashi, T. (2021). Novel Roles of Small Extracellular Vesicles in Regulating the Quiescence and Proliferation of Neural Stem Cells. Front Cell Dev Biol *9*, 762293. 10.3389/fcell.2021.762293.

73. Xiao, J., Zhao, T., Fang, W., Chen, Y., Wu, H., Li, P., Chen, X., Yan, R., Jiang, Y., Li, S., et al. (2022). Caveolin-1 signaling-driven mitochondrial fission and cytoskeleton remodeling promotes breast cancer migration. Int J Biochem Cell Biol *152*, 106307. 10.1016/j.biocel.2022.106307.

74. Vantaggiato, C., Castelli, M., Giovarelli, M., Orso, G., Bassi, M.T., Clementi, E., and De Palma, C. (2019). The Fine Tuning of Drp1-Dependent Mitochondrial Remodeling and Autophagy Controls Neuronal Differentiation. Front Cell Neurosci *13*, 120. 10.3389/fncel.2019.00120.

75. Bravo-Sagua, R., Parra, V., Ortiz-Sandoval, C., Navarro-Marquez, M., Rodriguez, A.E., Diaz-Valdivia, N., Sanhueza, C., Lopez-Crisosto, C., Tahbaz, N., Rothermel, B.A., et al. (2019). Caveolin-1 impairs PKA-DRP1-mediated remodelling of ER-mitochondria communication during the early phase of ER stress. Cell Death Differ *26*, 1195-1212. 10.1038/s41418-018-0197-1.

76. Bonds, J.A., Shetti, A., Stephen, T.K.L., Bonini, M.G., Minshall, R.D., and Lazarov, O. (2020). Deficits in hippocampal neurogenesis in obesity-dependent and -independent type-2 diabetes mellitus mouse models. Sci Rep *10*, 16368. 10.1038/s41598-020-73401-9.

77. Sandhu JK, R.-L.M., Abulrob A. (2021). Molecular and Functional Characterization of Caveolae in Mixed Cultures of Human NT-2 Neurons and Astrocytes. Neuroglia *2*, 68-88.

78. Yang, F., Shen, Y., Camp, D.G., 2nd, and Smith, R.D. (2012). High-pH reversed-phase chromatography with fraction concatenation for 2D proteomic analysis. Expert Rev Proteomics *9*, 129-134. 10.1586/epr.12.15.

79. Ashburner, M., Ball, C.A., Blake, J.A., Botstein, D., Butler, H., Cherry, J.M., Davis, A.P., Dolinski, K., Dwight, S.S., Eppig, J.T., et al. (2000). Gene ontology: tool for the unification of biology. The Gene Ontology Consortium. Nat Genet *25*, 25-29. 10.1038/75556.

80. Raudvere, U., Kolberg, L., Kuzmin, I., Arak, T., Adler, P., Peterson, H., and Vilo, J. (2019). g:Profiler: a web server for functional enrichment analysis and conversions of gene lists (2019 update). Nucleic Acids Res *47*, W191-W198. 10.1093/nar/gkz369.

81. Shannon, P., Markiel, A., Ozier, O., Baliga, N.S., Wang, J.T., Ramage, D., Amin, N., Schwikowski, B., and Ideker, T. (2003). Cytoscape: a software environment for integrated models of biomolecular interaction networks. Genome Res *13*, 2498-2504. 10.1101/gr.1239303.

82. Reimand, J., Isserlin, R., Voisin, V., Kucera, M., Tannus-Lopes, C., Rostamianfar, A., Wadi, L., Meyer, M., Wong, J., Xu, C., et al. (2019). Pathway enrichment analysis and visualization of omics data using g:Profiler, GSEA, Cytoscape and EnrichmentMap. Nat Protoc *14*, 482-517. 10.1038/s41596-018-0103-9.

83. Jiang, Y., Krantz, S., Qin, X., Li, S., Gunasekara, H., Kim, Y.M., Zimnicka, A., Bae, M., Ma, K., Toth, P.T., et al. (2022). Caveolin-1 controls mitochondrial damage and ROS production by regulating fission - fusion dynamics and mitophagy. Redox Biol *52*, 102304. 10.1016/j.redox.2022.102304.

84. Chaudhry, A., Shi, R., and Luciani, D.S. (2020). A pipeline for multidimensional confocal analysis of mitochondrial morphology, function, and dynamics in pancreatic beta-cells. Am J Physiol Endocrinol Metab *318*, E87-E101. 10.1152/ajpendo.00457.2019.

85. Xiong, Y., Wang, X.M., Zhong, M., Li, Z.Q., Wang, Z., Tian, Z.F., Zheng, K., and Tan, X.X. (2016). Alterations of caveolin-1 expression in a mouse model of delayed cerebral vasospasm following subarachnoid hemorrhage. Exp Ther Med *12*, 1993-2002. 10.3892/etm.2016.3568.

86. Kogo, H., and Fujimoto, T. (2000). Caveolin-1 isoforms are encoded by distinct mRNAs. Identification Of mouse caveolin-1 mRNA variants caused by alternative transcription initiation and splicing. FEBS Lett *465*, 119-123. 10.1016/s0014-5793(99)01730-5.

87. Nikolakopoulou, A.M., Wang, Y., Ma, Q., Sagare, A.P., Montagne, A., Huuskonen, M.T., Rege, S.V., Kisler, K., Dai, Z., Korbelin, J., et al. (2021). Endothelial LRP1 protects against neurodegeneration by blocking cyclophilin A. J Exp Med *218*. 10.1084/jem.20202207.

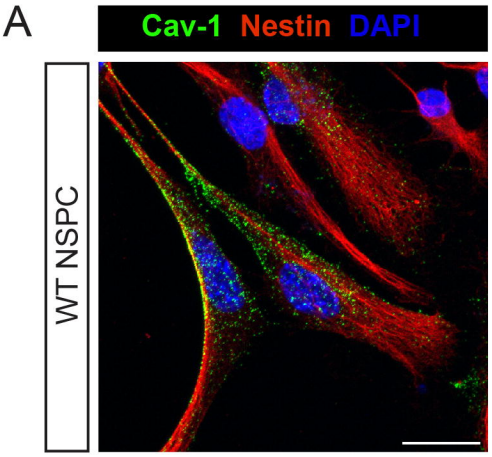
A
Cav-1 Nestin DAPI
WT NSPC

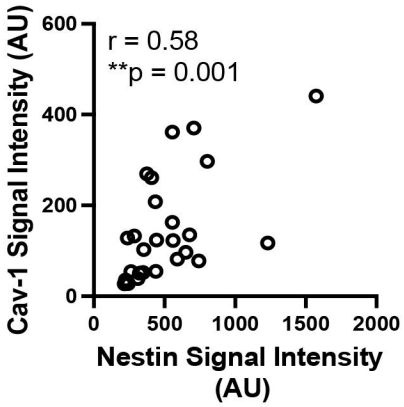
B
r = 0.58
**p = 0.001
Cav-1 Signal Intensity (AU)
Nestin Signal Intensity (AU)
0
200
400
600
0
500
1000
1500
2000

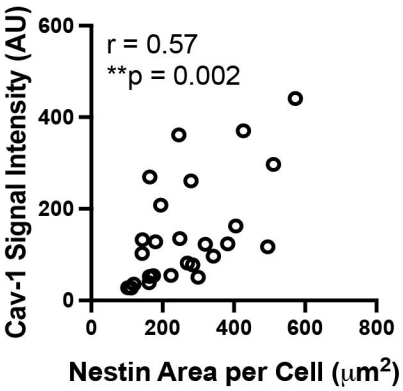
C
r = 0.57
**p = 0.002
Cav-1 Signal Intensity (AU)
Nestin Area per Cell (μm²)
0
200
400
600
0
200
400
600
800

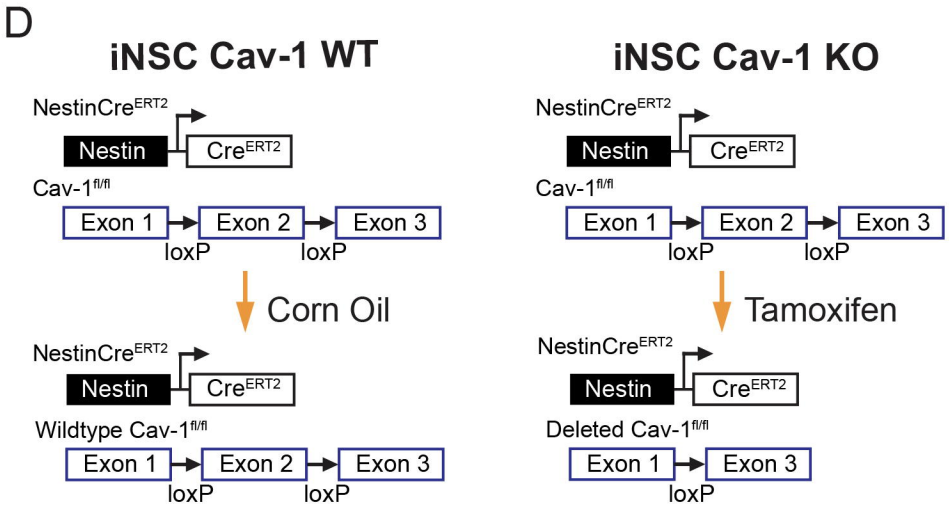
D
iNSC Cav-1 WT
NestinCreERT2
Nestin
CreERT2
Cav-1fl/fl
Exon 1
Exon 2
Exon 3
loxP
loxP
Corn Oil
NestinCreERT2
Nestin
CreERT2
Wildtype Cav-1fl/fl
Exon 1
Exon 2
Exon 3
loxP
loxP
iNSC Cav-1 KO
NestinCreERT2
Nestin
CreERT2
Cav-1fl/fl
Exon 1
Exon 2
Exon 3
loxP
loxP
Tamoxifen
NestinCreERT2
Nestin
CreERT2
Deleted Cav-1fl/fl
Exon 1
Exon 3
loxP

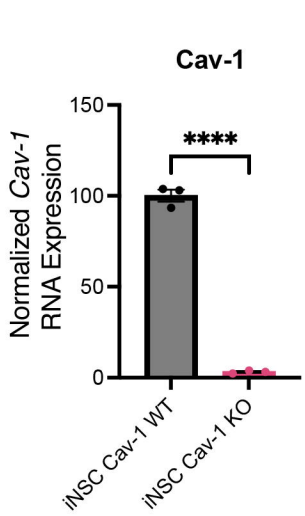
E
Cav-1
Normalized Cav-1 RNA Expression
****
150
100
50
0
iNSC Cav-1 WT
iNSC Cav-1 KO

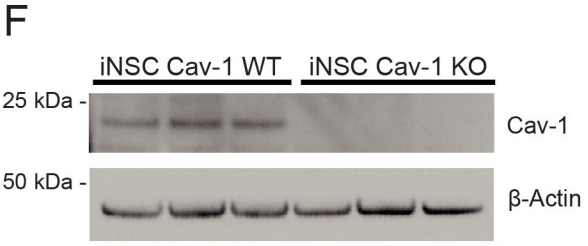
F
iNSC Cav-1 WT
iNSC Cav-1 KO
25 kDa -
Cav-1
50 kDa -
β-Actin

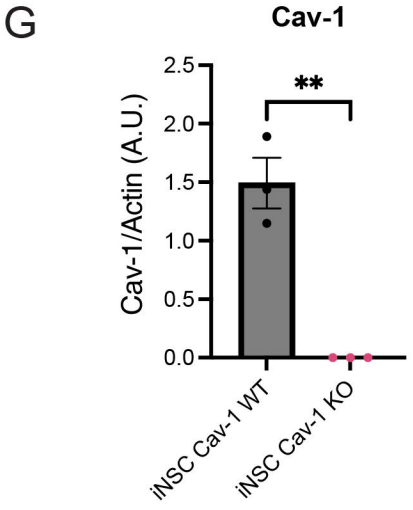
G
Cav-1
Cav-1/Actin (A.U.)
**
2.5
2.0
1.5
1.0
0.5
0.0
iNSC Cav-1 WT
iNSC Cav-1 KO

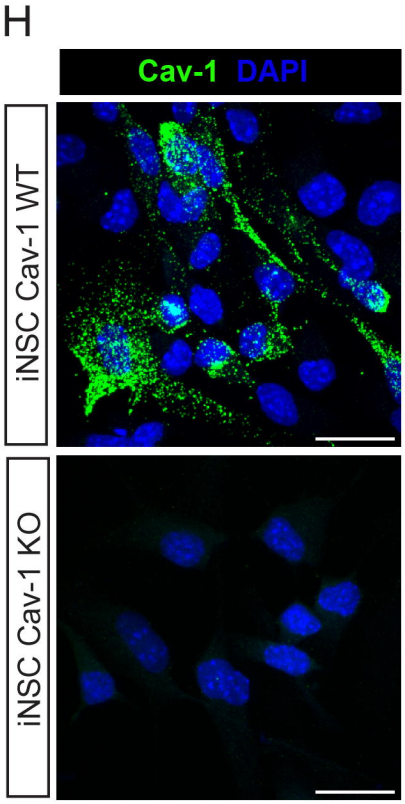
H
Cav-1 DAPI
iNSC Cav-1 WT
iNSC Cav-1 KO

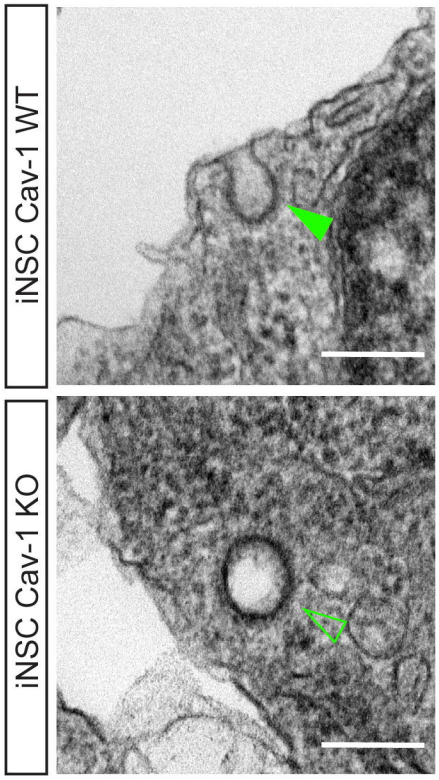
I
iNSC Cav-1 WT
iNSC Cav-1 KO

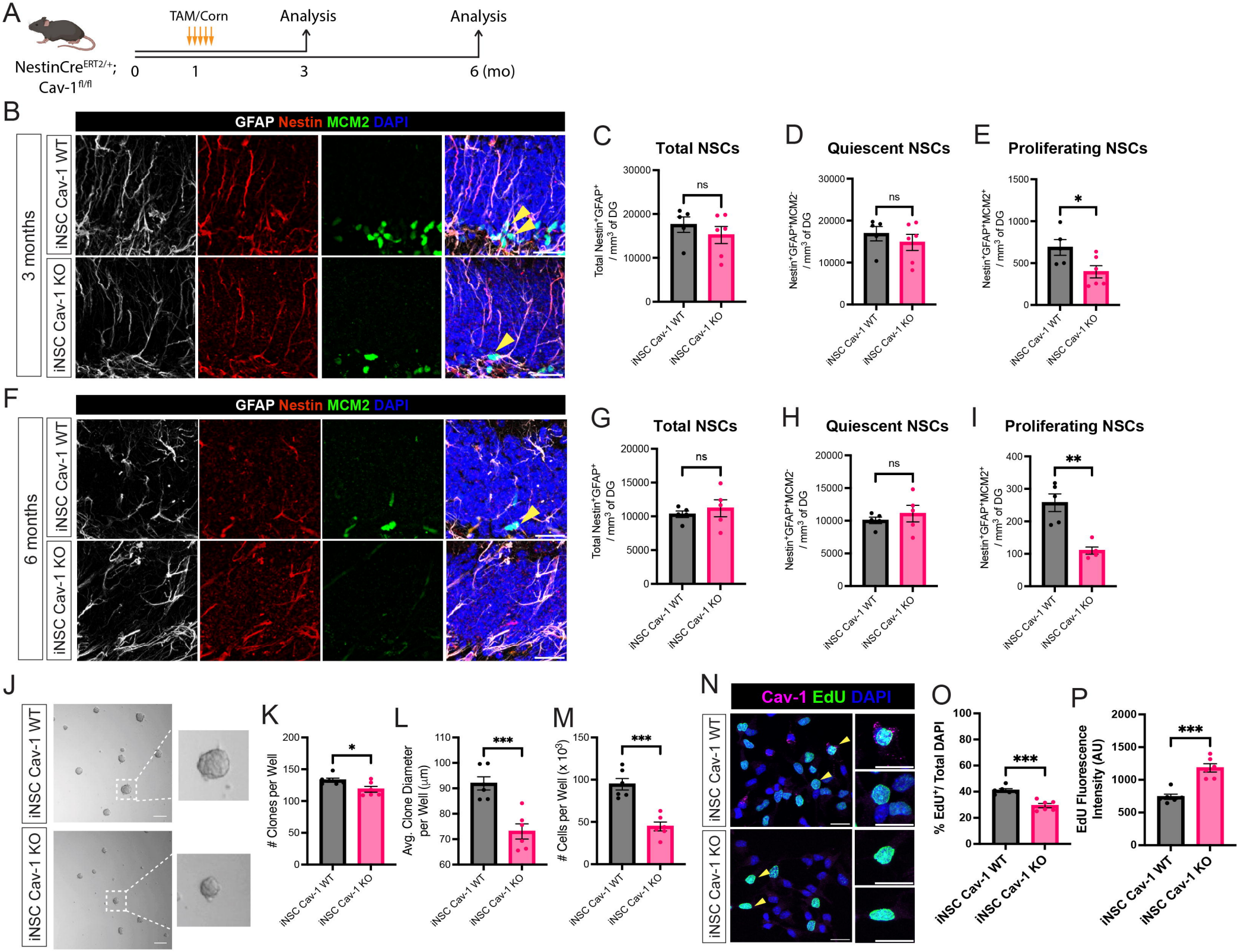
A
NestinCre$^{ERT2/+}$; Cav-1$^{fl/fl}$
TAM/Corn
Analysis
Analysis
0
1
3
6 (mo)
B
GFAP Nestin MCM2 DAPI
3 months
iNSC Cav-1 WT
iNSC Cav-1 KO
C
Total NSCs
Total Nestin$^+$GFAP$^+$ / mm^3 of DG
ns
D
Quiescent NSCs
Nestin$^+$GFAP$^+$MCM2$^-$ / mm^3 of DG
ns
E
Proliferating NSCs
Nestin$^+$GFAP$^+$MCM2$^+$ / mm^3 of DG
*
F
GFAP Nestin MCM2 DAPI
6 months
iNSC Cav-1 WT
iNSC Cav-1 KO
G
Total NSCs
Total Nestin$^+$GFAP$^+$ / mm^3 of DG
ns
H
Quiescent NSCs
Nestin$^+$GFAP$^+$MCM2$^-$ / mm^3 of DG
ns
I
Proliferating NSCs
Nestin$^+$GFAP$^+$MCM2$^+$ / mm^3 of DG
**
J
iNSC Cav-1 WT
iNSC Cav-1 KO
K
Clones per Well
*
L
Avg. Clone Diameter per Well (μm)
***
M
Cells per Well (x 10^3)
***
N
Cav-1 EdU DAPI
iNSC Cav-1 WT
iNSC Cav-1 KO
O
% EdU$^+$/ Total DAPI
***
P
EdU Fluorescence Intensity (AU)
***

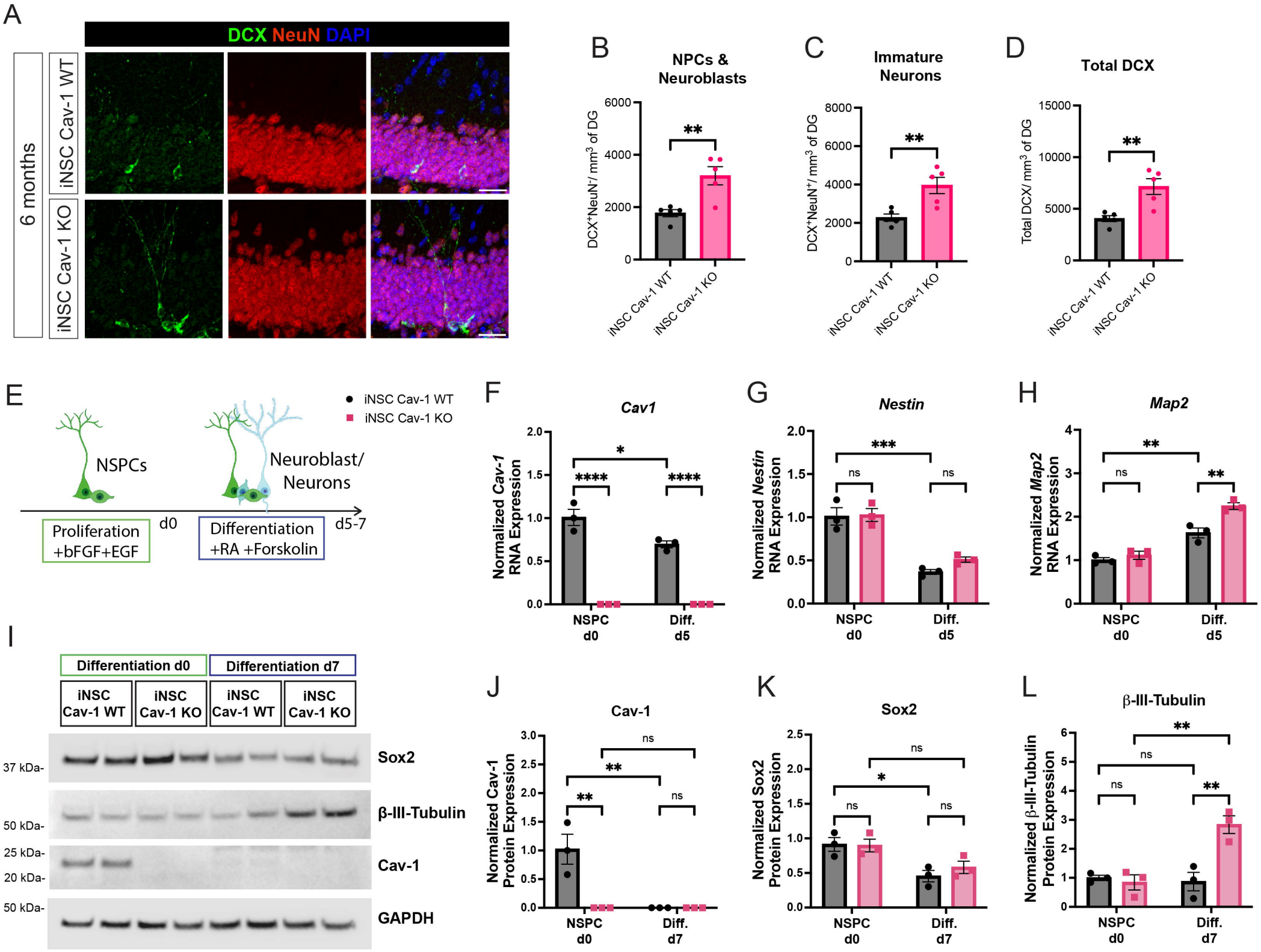
A
DCX NeuN DAPI
6 months
iNSC Cav-1 WT
iNSC Cav-1 KO
B
NPCs & Neuroblasts
DCX+NeuN-/ mm3 of DG
6000
4000
2000
0
**
iNSC Cav-1 WT
iNSC Cav-1 KO
C
Immature Neurons
DCX+NeuN+/ mm3 of DG
8000
6000
4000
2000
0
**
iNSC Cav-1 WT
iNSC Cav-1 KO
D
Total DCX
Total DCX/ mm3 of DG
15000
10000
5000
0
**
iNSC Cav-1 WT
iNSC Cav-1 KO
E
iNSC Cav-1 WT
iNSC Cav-1 KO
NSPCs
Neuroblast/ Neurons
d0
d5-7
Proliferation +bFGF+EGF
Differentiation +RA +Forskolin
F
Cav1
Normalized Cav-1 RNA Expression
2.0
1.5
1.0
0.5
0.0
*
****
****
NSPC d0
Diff. d5
G
Nestin
Normalized Nestin RNA Expression
2.0
1.5
1.0
0.5
0.0
***
ns
ns
NSPC d0
Diff. d5
H
Map2
Normalized Map2 RNA Expression
4
3
2
1
0
**
ns
**
NSPC d0
Diff. d5
I
Differentiation d0
Differentiation d7
iNSC Cav-1 WT
iNSC Cav-1 KO
iNSC Cav-1 WT
iNSC Cav-1 KO
37 kDa-
Sox2
50 kDa-
β-III-Tubulin
25 kDa-
20 kDa-
Cav-1
50 kDa-
GAPDH
J
Cav-1
Normalized Cav-1 Protein Expression
3.0
2.5
2.0
1.5
1.0
0.5
0.0
ns
**
**
ns
NSPC d0
Diff. d7
K
Sox2
Normalized Sox2 Protein Expression
2.5
2.0
1.5
1.0
0.5
0.0
ns
*
ns
ns
NSPC d0
Diff. d7
L
β-III-Tubulin
Normalized β-III-Tubulin Protein Expression
6
5
4
3
2
1
0
**
ns
ns
**
NSPC d0
Diff. d7

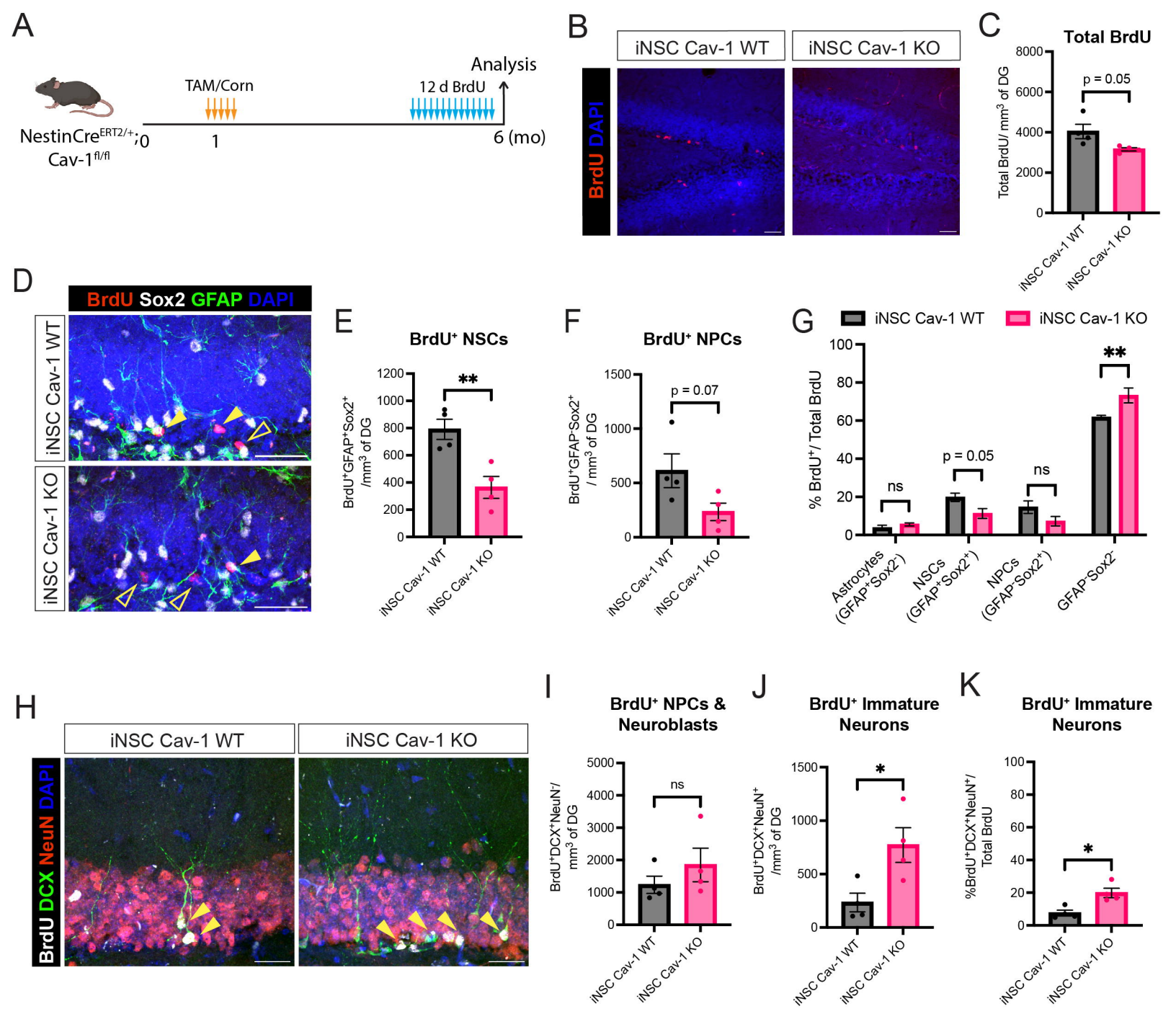
A
NestinCre$^{ERT2/+}$; Cav-1$^{fl/fl}$
TAM/Corn
12 d BrdU
Analysis
0
1
6 (mo)
B
iNSC Cav-1 WT
iNSC Cav-1 KO
BrdU DAPI
C
Total BrdU
Total BrdU/ mm^3 of DG
p = 0.05
iNSC Cav-1 WT
iNSC Cav-1 KO
D
BrdU Sox2 GFAP DAPI
iNSC Cav-1 WT
iNSC Cav-1 KO
E
BrdU$^+$ NSCs
BrdU$^+$GFAP$^+$Sox2$^+$ /mm^3 of DG
**
F
BrdU$^+$ NPCs
BrdU$^+$GFAP$^-$Sox2$^+$ / mm^3 of DG
p = 0.07
G
iNSC Cav-1 WT
iNSC Cav-1 KO
% BrdU$^+$/ Total BrdU
ns
p = 0.05
ns
**
Astrocytes (GFAP$^+$Sox2$^-$)
NSCs (GFAP$^+$Sox2$^+$)
NPCs (GFAP$^-$Sox2$^+$)
GFAP$^-$Sox2$^-$
H
iNSC Cav-1 WT
iNSC Cav-1 KO
BrdU DCX NeuN DAPI
I
BrdU$^+$ NPCs & Neuroblasts
BrdU$^+$DCX$^+$NeuN$^-$/ mm^3 of DG
ns
J
BrdU$^+$ Immature Neurons
BrdU$^+$DCX$^+$NeuN$^+$ /mm^3 of DG
*
K
BrdU$^+$ Immature Neurons
%BrdU$^+$DCX$^+$NeuN$^+$/ Total BrdU
*

A

Context Discrimmination

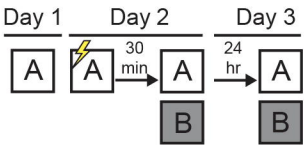

B

Day 2
30 min Post-Shock

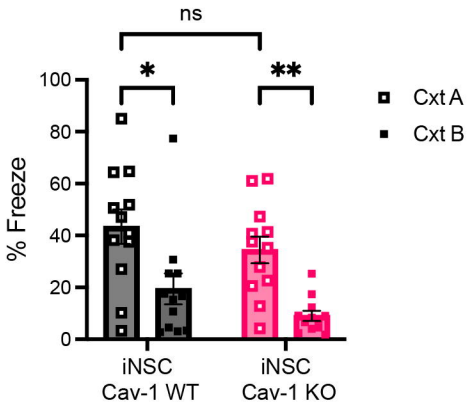

C

Day 2
30 min Post-Shock

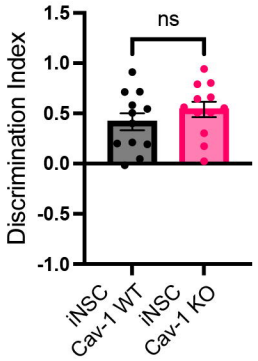

D

Day 3
24 hr Post-Shock

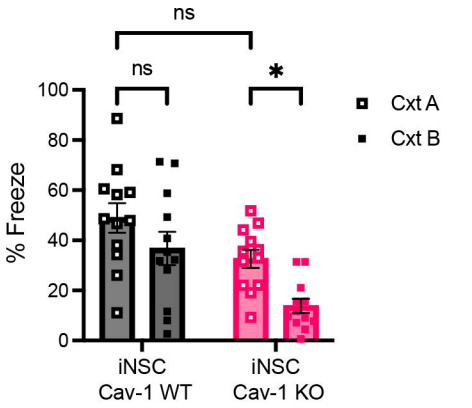

E

Day 3
24 hr Post-Shock

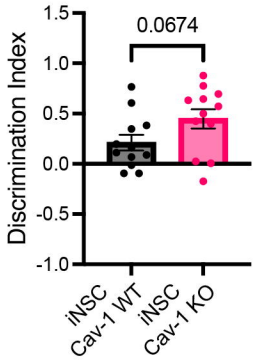

F

Context Generalization

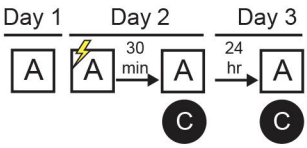

G

Day 2
30 min Post-Shock

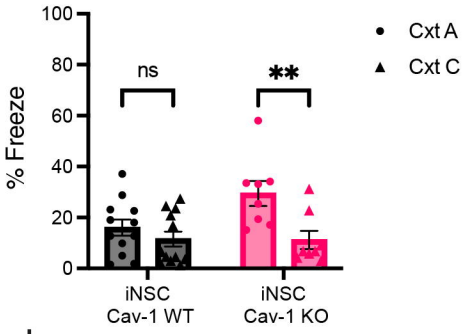

H

Day 2
30 min Post-Shock

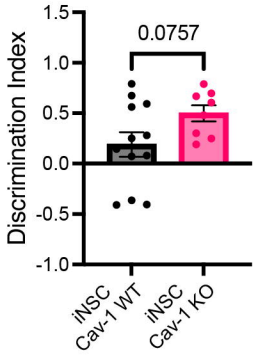

I

Day 3
24 hr Post-Shock

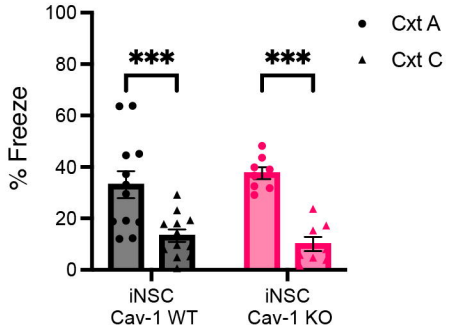

J

Day 3
24 hr Post-Shock

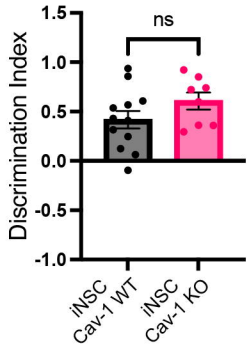

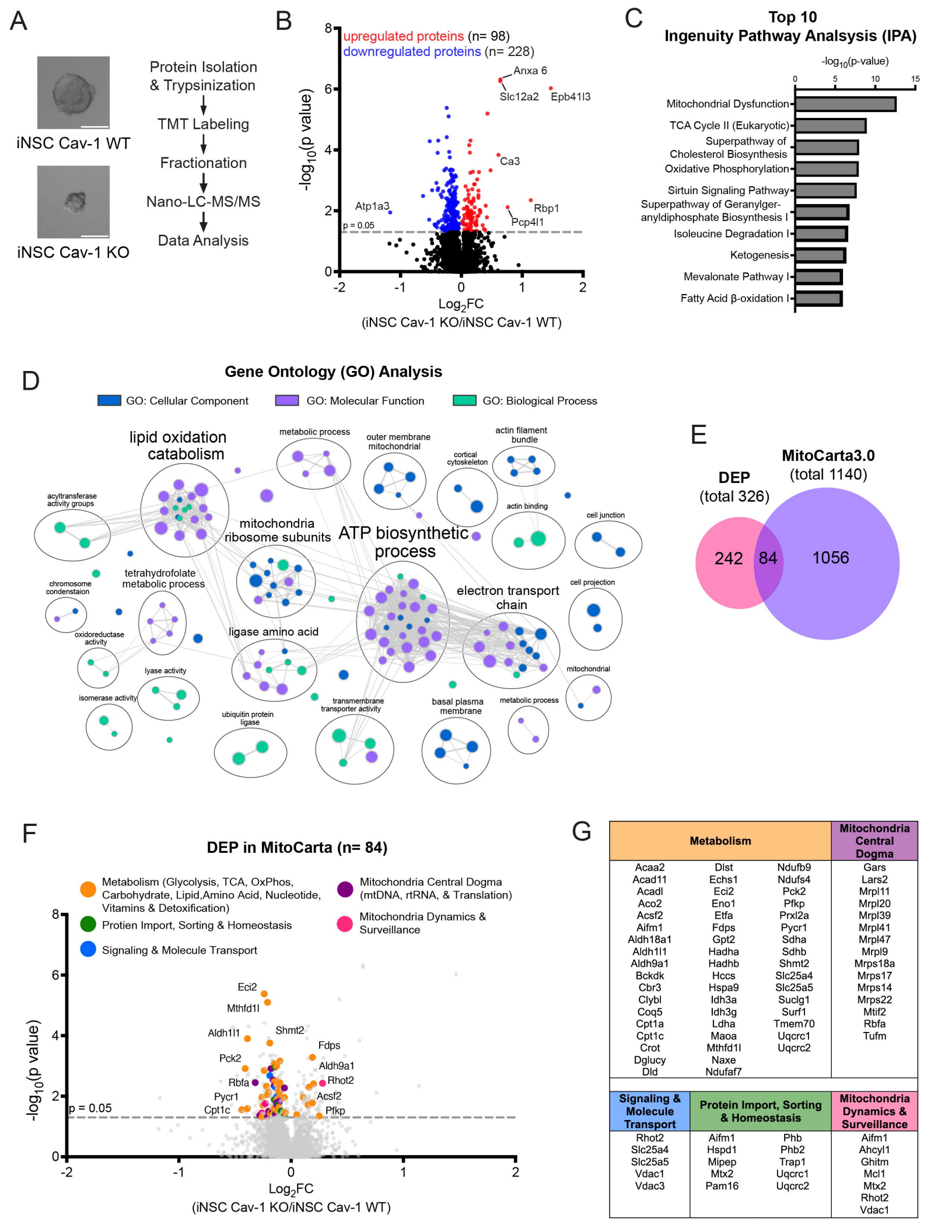
A
iNSC Cav-1 WT
iNSC Cav-1 KO
Protein Isolation & Trypsinization
TMT Labeling
Fractionation
Nano-LC-MS/MS
Data Analysis
B
upregulated proteins (n= 98)
downregulated proteins (n= 228)
Anxa 6
Slc12a2
Epb41l3
Ca3
Atp1a3
Rbp1
Pcp4l1
p = 0.05
-log10(p value)
Log2FC
(iNSC Cav-1 KO/iNSC Cav-1 WT)
C
Top 10
Ingenuity Pathway Analsysis (IPA)
-log10(p-value)
Mitochondrial Dysfunction
TCA Cycle II (Eukaryotic)
Superpathway of Cholesterol Biosynthesis
Oxidative Phosphorylation
Sirtuin Signaling Pathway
Superpathway of Geranylger-anyldiphosphate Biosynthesis I
Isoleucine Degradation I
Ketogenesis
Mevalonate Pathway I
Fatty Acid β-oxidation I
D
Gene Ontology (GO) Analysis
GO: Cellular Component
GO: Molecular Function
GO: Biological Process
lipid oxidation catabolism
metabolic process
outer membrane mitochondrial
actin filament bundle
cortical cytoskeleton
acyltransferase activity groups
actin binding
cell junction
mitochondria ribosome subunits
ATP biosynthetic process
tetrahydrofolate metabolic process
chromosome condenstaion
electron transport chain
cell projection
oxidoreductase activity
ligase amino acid
lyase activity
mitochondrial
isomerase activity
transmembrane transporter activity
basal plasma membrane
metabolic process
ubiquitin protein ligase
E
DEP
(total 326)
MitoCarta3.0
(total 1140)
242
84
1056
F
DEP in MitoCarta (n= 84)
Metabolism (Glycolysis, TCA, OxPhos, Carbohydrate, Lipid,Amino Acid, Nucleotide, Vitamins & Detoxification)
Protien Import, Sorting & Homeostasis
Signaling & Molecule Transport
Mitochondria Central Dogma (mtDNA, rtRNA, & Translation)
Mitochondria Dynamics & Surveillance
Eci2
Mthfd1l
Aldh1l1
Shmt2
Fdps
Pck2
Aldh9a1
Rbfa
Rhot2
Pycr1
Acsf2
Cpt1c
Pfkp
p = 0.05
-log10(p value)
Log2FC
(iNSC Cav-1 KO/iNSC Cav-1 WT)
G
Metabolism
Acaa2 Acad11 Acadl Aco2 Acsf2 Aifm1 Aldh18a1 Aldh1l1 Aldh9a1 Bckdk Cbr3 Clybl Coq5 Cpt1a Cpt1c Crot Dglucy Dld
Dlst Echs1 Eci2 Eno1 Etfa Fdps Gpt2 Hadha Hadhb Hccs Hspa9 Idh3a Idh3g Ldha Maoa Mthfd1l Naxe Ndufaf7
Ndufb9 Ndufs4 Pck2 Pfkp Prxl2a Pycr1 Sdha Sdhb Shmt2 Slc25a4 Slc25a5 Suclg1 Surf1 Tmem70 Uqcrc1 Uqcrc2
Mitochondria Central Dogma
Gars Lars2 Mrpl11 Mrpl20 Mrpl39 Mrpl41 Mrpl47 Mrpl9 Mrps18a Mrps17 Mrps14 Mrps22 Mtif2 Rbfa Tufm
Signaling & Molecule Transport
Rhot2 Slc25a4 Slc25a5 Vdac1 Vdac3
Protein Import, Sorting & Homeostasis
Aifm1 Hspd1 Mipep Mtx2 Pam16
Phb Phb2 Trap1 Uqcrc1 Uqcrc2
Mitochondria Dynamics & Surveillance
Aifm1 Ahcyl1 Ghitm Mcl1 Mtx2 Rhot2 Vdac1

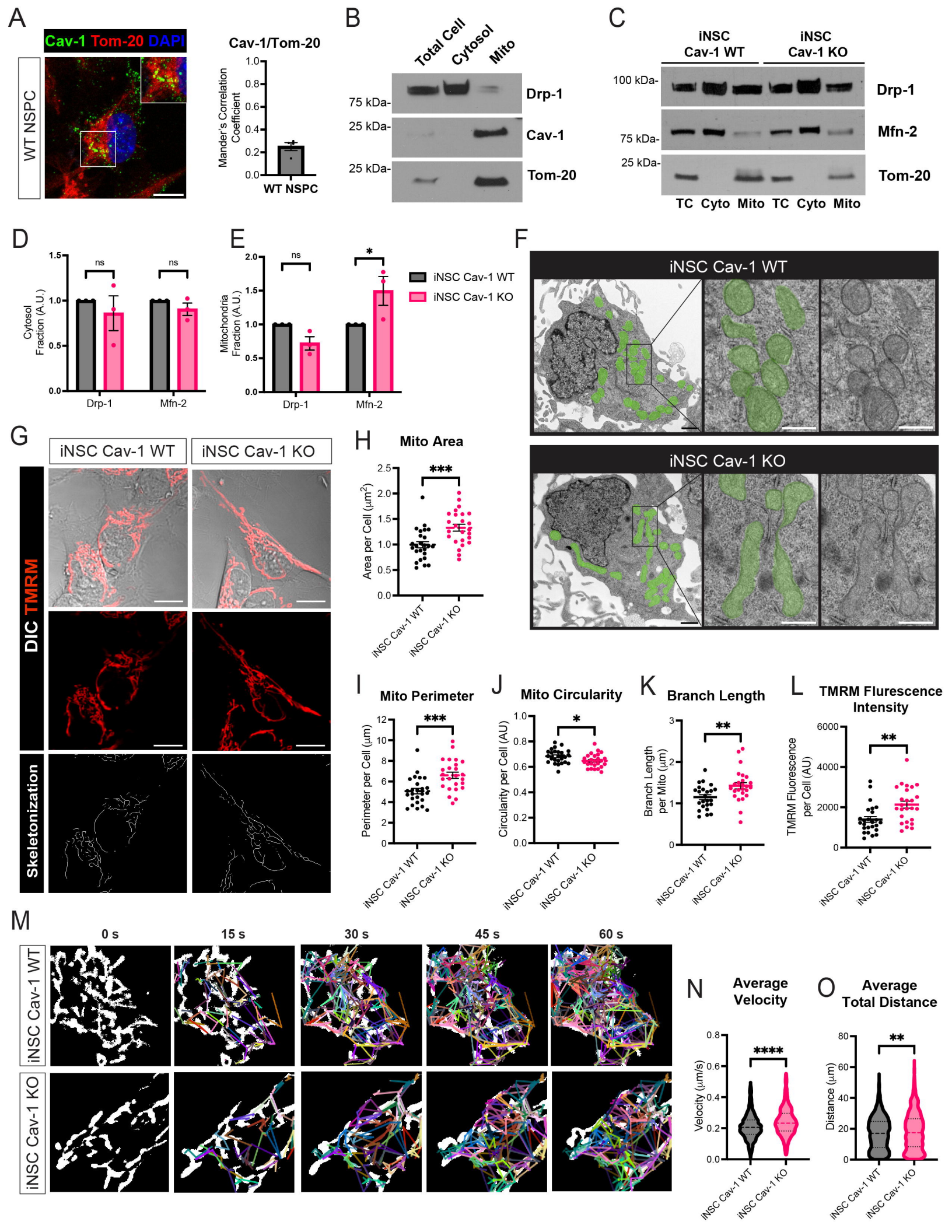
A
Cav-1 Tom-20 DAPI
WT NSPC
Cav-1/Tom-20
Mander's Correlation Coefficient
WT NSPC
B
Total Cell
Cytosol
Mito
75 kDa-
25 kDa-
25 kDa-
Drp-1
Cav-1
Tom-20
C
iNSC Cav-1 WT
iNSC Cav-1 KO
100 kDa-
75 kDa-
25 kDa-
Drp-1
Mfn-2
Tom-20
TC Cyto Mito TC Cyto Mito
D
Cytosol Fraction (A.U.)
ns
ns
Drp-1
Mfn-2
E
Mitochondria Fraction (A.U.)
ns
*
Drp-1
Mfn-2
iNSC Cav-1 WT
iNSC Cav-1 KO
F
iNSC Cav-1 WT
iNSC Cav-1 KO
G
iNSC Cav-1 WT
iNSC Cav-1 KO
DIC TMRM
Skeletonization
H
Mito Area
Area per Cell (μm²)
***
iNSC Cav-1 WT
iNSC Cav-1 KO
I
Mito Perimeter
Perimeter per Cell (μm)
***
J
Mito Circularity
Circularity per Cell (AU)
*
K
Branch Length
Branch Length per Mito (μm)
**
L
TMRM Flurescence Intensity
TMRM Fluorescence per Cell (AU)
**
M
0 s
15 s
30 s
45 s
60 s
iNSC Cav-1 WT
iNSC Cav-1 KO
N
Average Velocity
Velocity (μm/s)
****
O
Average Total Distance
Distance (μm)
**